

Aircraft-derived particle fluxes distinguish entrainment zone and decoupled layer nucleation in marine boundary layers

Ajmal Rasheeda Satheesh¹, Markus D. Petters², and Nicholas Meskhidze¹

¹Department of Marine, Earth, and Atmospheric Sciences, North Carolina State University, Raleigh, NC 27695, USA.

²Department of Chemical and Environmental Engineering, University of California, Riverside, CA 92521, USA.

Corresponding author: Nicholas Meskhidze (nmeskhidze@ncsu.edu)

Abstract

The vertical distribution of freshly nucleated aerosol particles in the marine boundary layer remains poorly constrained, limiting our ability to represent new particle formation in climate models. Here we characterize 3–10 nm particle events, termed small particle events (SPEs), by deriving their vertical turbulent fluxes from aircraft measurements during the Aerosol and Cloud Experiments in the Eastern North Atlantic (ACE-ENA) campaign. To overcome stationarity limitations of traditional eddy covariance methods, we applied continuous wavelet transform analysis to data collected during June–July 2017 and January–February 2018 flights over the Azores. Our flux-based analysis revealed two distinct SPE scenarios with different vertical structures and spatial extents. The first featured nucleation in the entrainment zone, where free tropospheric air entrains into the boundary layer. The second showed nucleation in the decoupled layer, a stratified region between the well-mixed surface layer and cloud-topped upper boundary layer. In both cases, convergence of air masses from different layers diluted preexisting aerosol surface area to very low levels, creating conditions favorable for nucleation and generating strong downward particle fluxes. SPEs occurred in 15% of flights, challenging prevailing theoretical expectations that new particle formation should rarely occur in marine boundary layers due to high condensation and coagulation sink capacity of sea spray aerosols. Aircraft-derived particle fluxes provide first observational constraints on the vertical location and source strength of likely nucleation regions in the remote marine boundary layer, improving aerosol source representations in climate models and reducing uncertainties in aerosol-cloud interactions.

1. Introduction

Cloud adjustments due to aerosols constitute one of the most significant uncertainties in climate modeling (Intergovernmental Panel on Climate Change (IPCC), 2023). The magnitude of anthropogenic aerosol radiative forcing over the industrial period is strongly influenced by the abundance and properties of natural aerosols (Andreae, 2007; Carslaw et al., 2013; Hoose et al., 2009; Meskhidze et al., 2011). While uncertainties in aerosol radiative forcing from different processes (emissions, long-range transport, new particle formation, and removal) vary spatially, marine boundary layer (MBL) cloud microphysical properties exhibit the highest sensitivity to aerosol changes (Bellouin et al., 2020; Zhang et al., 2024). Understanding how marine low level clouds and their radiative effects respond to changing aerosol load is important due to their extensive spatial coverage, low optical thickness, and low background cloud condensation nuclei (CCN) concentrations. The response of these clouds to changes in aerosol loading remains

34 poorly constrained and represents a key source of uncertainty in climate projections (Zhang et al., 2024).
35 Consequently, understanding aerosol composition, dynamics, and the mechanisms controlling CCN number budgets
36 within the MBL is critical for improving climate models and reducing predictive uncertainties. While freshly nucleated
37 particles in the 3–10 nm size range must undergo substantial growth before reaching CCN-relevant sizes (>50–80
38 nm), this growth pathway is well established in marine environments. At typical marine boundary layer growth rates
39 of 1–3 nm hr⁻¹ (Ehn et al., 2010; Nieminen et al., 2018; O’Dowd et al., 2010; Zheng et al., 2018), newly formed
40 particles can reach CCN sizes within 24–48 hours. This timescale is consistent with air mass residence times in the
41 remote marine boundary layer (Kulmala et al., 2012; Zheng et al., 2021). Constraining the vertical location and flux
42 magnitude of freshly nucleated particles therefore represents a critical first step toward understanding the full aerosol
43 number budget in marine environments, including the ultimate contribution of NPF to CCN populations.

44 Previous studies have identified three primary aerosol sources in remote MBLs: (1) long-range continental transport
45 (Logan et al., 2014), (2) downward mixing of particles formed in the free troposphere (FT) through new particle
46 formation (NPF) mechanisms (Clarke et al., 2013), and (3) sea spray emissions (Quinn et al., 2017). NPF occurring
47 either near the top of stratocumulus cloud decks within open-cell regions (Petters et al., 2006) or in the upper portions
48 of mid-latitude MBLs (Zheng et al., 2021) has been suggested as an important in-situ aerosol source within the MBL.
49 However, the difficulty in capturing actual nucleation events and determining their precise vertical location has led to
50 the prevailing theoretical view that NPF should rarely occur in remote marine boundary layers over open oceans. This
51 expectation is based on the high condensation and coagulation sink capacity of the remote MBL, which includes not
52 only sea spray aerosols (Bates et al., 1998; Pirjola et al., 2000) but also accumulation-mode sulfate and organic
53 particles entrained from the free troposphere (Yoon and Brimblecombe, 2002). Clouds further suppress NPF by
54 scavenging Aitken-mode particles (Zheng et al., 2018), accelerating sulfate production on existing droplets through
55 aqueous-phase SO₂ oxidation (Sanchez et al., 2021), and sequestering DMS oxidation products such as
56 Hydroperoxymethyl thioformate (HPMTF) that would otherwise contribute to sulfuric acid formation (Novak et al.,
57 2021). Independent corroboration of in-situ NPF over the eastern North Atlantic comes from the Azores
58 Stratocumulus Measurements of Radiation, Turbulence and Aerosols (ACORES) campaign, which conducted
59 helicopter-borne observations over Graciosa Island in July 2017, overlapping in time and location with the ACE-ENA
60 campaign analyzed here. Siebert et al., (2021) reported frequent burst-like freshly nucleated particle events near the
61 stratocumulus cloud top and in the free troposphere, while also noting that these particles did not grow to CCN-
62 relevant sizes within the ~2-hour observation window. This outcome is expected given the 24–48 hour growth
63 timescales discussed above. These concentration-based observations, however, could not determine the precise
64 vertical location of the nucleation source regions, motivating the flux-based approach developed in the present study.

65 Determining the vertical origin of freshly nucleated particles, whether from the free troposphere, the interfacial layer
66 near the marine boundary layer–free troposphere boundary, or the interface between the well-mixed marine boundary
67 layer and decoupled layer, has critical implications for both fundamental understanding and climate modeling.
68 Knowledge of where nucleation occurs is essential for understanding aerosol formation mechanisms and enabling
69 climate models to accurately simulate aerosol number size distributions required for radiative calculations. Most
70 atmospheric models have historically assumed that nucleation should be negligible in marine boundary layers, instead

71 predicting that particle formation would be favored at high altitudes where both temperature and aerosol surface area
72 are substantially lower. However, traditional time-averaged aerosol concentration measurements from aircraft
73 campaigns provide limited information about the precise vertical location where nucleation events occur. This
74 limitation has prevented definitive identification of nucleation zones within the marine boundary layer and hampered
75 efforts to constrain the relative importance of different aerosol sources to marine aerosol budgets. Without direct
76 observational evidence of where particles form, climate models continue to rely on theoretical assumptions that may
77 not accurately represent actual nucleation processes in marine environments.

78 To address this critical knowledge gap, vertical turbulent flux measurements of freshly nucleated 3–10 nm particles
79 have emerged as particularly valuable tools for inferring the vertical location of likely nucleation source regions (Islam
80 et al., 2022). The flux direction provides indirect evidence of the likely nucleation location: positive (upward) fluxes
81 indicate nucleation below the aircraft, while negative (downward) fluxes suggest nucleation above the aircraft. This
82 approach offers unprecedented spatial and temporal resolution for identifying nucleation zones that cannot be detected
83 through conventional concentration measurements alone. In this study, we derive vertical turbulent fluxes of 3–10 nm
84 particles using data collected during the Aerosol and Cloud Experiments in the Eastern North Atlantic (ACE-ENA)
85 campaign. The campaign comprised two intensive operational periods (IOPs) – summer 2017 and winter 2018 –
86 utilizing the G1 research aircraft from the DOE Atmospheric Radiation Measurement (ARM) program. By applying
87 continuous wavelet transform techniques to high-frequency aircraft measurements, we provide the first flux-based
88 observational constraints on the vertical distribution of likely NPF source regions in remote marine boundary layers,
89 enabling improved representation of aerosol sources in climate models.

90 **2. Materials and Methods**

91 **2.1 Sampling Site**

92 The Department of Energy Atmospheric Radiation Measurement (DOE–ARM) Eastern North Atlantic (ENA) facility
93 is positioned on Graciosa Island within the Azores archipelago, located in the northeastern Atlantic Ocean to the west
94 of Portugal (Mather and Voyles, 2013). Air mass transport to this location follows four main pathways: (1) polluted
95 outflow from North American sources, (2) continental emissions originating from northern European regions, (3)
96 relatively clean Arctic air masses, and (4) air masses that recirculate within the Azores High pressure system (Wood
97 et al., 2015; Zheng et al., 2018). The location is characterized by a low average annual aerosol optical depth (AOD)
98 of 0.12 (Logan et al., 2014).

99 Data collection for this research occurred during the ACE-ENA field campaign, which included two intensive
100 observation periods (IOPs): the initial period ran from June 21 to July 20, 2017, while the second period extended
101 from January 15 to February 18, 2018 (Wang et al., 2019). All data from the ARM ENA site are publicly accessible
102 through the ARM Data Discovery tool.

103 2.2 Instrumentation

104 This study utilized datasets from the ARM Aerial Facility (Schmid et al., 2014). The G-1 research aircraft was
105 equipped with over 50 instruments for comprehensive measurements of aerosols, clouds, and atmospheric processes.
106 Detailed information regarding flight patterns executed during the campaign can be found in (Wang et al., 2019).

107 Two Condensation Particle Counters (CPCs, models 3025A and 3772, TSI Inc.) with nominal 50% counting efficiency
108 cutoff diameters of 3 nm and 10 nm, respectively, sampled through an isokinetic inlet exhibiting >90% efficiency for
109 particles with aerodynamic diameters below 5 μm . The concentration of 3–10 nm sized particles was calculated as the
110 difference between these CPC measurements and is denoted as N_{3-10} throughout this paper. Since the measurements
111 did not extend to particle sizes small enough to directly identify nucleation events, we follow (Islam et al., 2022) in
112 using the term "small particle event" (SPE) to characterize these observations. The CPC 3772 operated at a constant
113 1 LPM flow rate maintained by an external pump and critical orifice (Fan and Pekour, 2018), while the CPC 3025A
114 sample flow rate was not actively controlled. Both flow rates remained stable across the sampling altitude range
115 (Zheng et al., 2021). The airborne CPC configuration was validated for operation up to 4000 m altitude and across
116 ambient relative humidity conditions of 0–90% RH. For a typical polluted environment ($\sim 5000 \text{ cm}^{-3}$), CPC
117 concentration measurements had an accuracy of 0.3 % (Kuang and Mei, 2019). All data used in this study passed
118 instrument mentor specified quality control filters, which are distributed alongside the data.

119 Vertical wind speed (w) was measured using the Aircraft Integrated Meteorological Measurement System probe
120 (AIMMS–20, Aiventech Research Inc.). The raw measurements define downward movement as positive; therefore,
121 the sign was inverted to align with meteorological convention (positive values indicating updrafts and negative values
122 indicating downdrafts). Although measurements were recorded at 20 Hz, they were downsampled to 1 Hz to match
123 the temporal resolution of the CPC data acquisition.

124 Aerosol size distributions from 10 nm to 600 nm were characterized using a Fast Integrated Mobility Spectrometer
125 (FIMS) (Kulkarni and Wang, 2006a, b). The FIMS provides size distribution measurements at 1-second temporal
126 resolution suitable for detecting both remote continental and clean marine aerosol concentrations, as demonstrated in
127 aircraft-based deployments (Kulkarni and Wang, 2006a, b; Olfert et al., 2008). Particles are charged within the
128 instrument and separated by electrical mobility using an applied electric field. The separated particles are subsequently
129 grown into supermicron droplets in a condenser and imaged with a high-speed camera. This approach enables the
130 FIMS to deliver size distribution measurements comparable to those of Scanning Mobility Particle Sizers (SMPS),
131 but at a significantly higher time resolution. This study employed an advanced FIMS configuration utilizing a spatially
132 varying electric field that extends the measurement range from 10 nm to 600 nm (Wang et al., 2017b, a). Size
133 distribution measurements were normalized to dry conditions; therefore, reported size distributions and number
134 concentrations do not represent ambient humidity conditions. Cloud contamination filters were applied to prevent
135 misclassification of cloud droplets as aerosol particles, with detailed filtering procedures described in the following
136 section. FIMS-derived number concentration also served as a quality control flag for the CPC 3772. Since both
137 instruments share an overlapping detection size range (10–600 nm for FIMS; >10 nm for CPC 3772), their total
138 number concentrations should be broadly comparable, with CPC showing a higher total number concentration than
139 FIMS under normal operating conditions, as the CPC detects all particles above 10 nm while FIMS is bounded at 600

140 nm. The histogram of differences between CPC and integral FIMS concentrations (Fig. S1) shows a distribution
141 sharply peaked near zero with a slight negative skew, confirming good agreement during normal operation. The dashed
142 red line indicates zero difference, below which CPC concentrations are physically implausible given the instruments'
143 overlapping but non-identical size ranges. The negative tail reflects episodic periods when the CPC concentration was
144 found to be suspect, likely due to working fluid depletion or a change in flow rate controlled by a critical orifice,
145 producing sustained negative deviations that are physically implausible given the instruments' overlapping size ranges.
146 These episodic malfunctions are distinct from the instrument's typical 0.3% measurement accuracy under stable
147 conditions (Kuang and Mei, 2019). Hence, a conservative threshold was set with CPC concentrations falling below
148 10% of the simultaneously measured FIMS concentration, indicating a physically implausible discrepancy
149 inconsistent with real atmospheric variability, and were therefore excluded from analysis as likely instrument
150 malfunctions.

151 A two-dimensional stereo probe (2D-S) was used to retrieve drizzle concentration. It uses shadowgraphy to measure
152 size distribution of hydrometeor particles in the size range 15 μm to 2.5 mm (Glienke and Mei, 2019). All data
153 products are publicly available through the ARM DOE website with citations in the data availability section and have
154 undergone quality control by instrument mentors. Additional technical details are available in the corresponding
155 citations.

156 **2.3 Data Reduction**

157 **2.3.1 Droplet shattering and cloud contamination**

158 Droplet shattering represents a significant source of measurement contamination in airborne aerosol sampling studies.
159 Weber et al., (1998) described this phenomenon as the fragmentation of cloud droplets during in-cloud measurements,
160 which can produce artifacts as small as 3 nm that appear in sampling instruments. Similarly, Korolev and Isaac, (2005)
161 documented comparable shattering effects with ice particles. While a detailed examination of the physical mechanisms
162 behind droplet shattering lies beyond this study's scope, it is essential to filter such artifacts from our dataset to prevent
163 misidentification of SPEs.

164 Cloud contamination was systematically detected and eliminated by calculating liquid water content (LWC) using the
165 approach of Zheng et al., (2021), which utilizes droplet size spectra from the Fast Cloud Droplet Probe (FCDP). Visual
166 data examination established a detection threshold of $3 \times 10^{-3} \text{ g m}^{-3}$, comparable to the 10^{-3} g m^{-3} threshold employed
167 by Zheng et al., (2021). Data exceeding this LWC threshold were excluded from analysis.

168 **2.3.2 Time lag correction**

169 Accurate temporal alignment between the vertical wind speed measured by the AIMMS-20 probe and the particle
170 concentration measured by the CPCs is essential for reliable flux calculations. Because these instruments were located
171 at different positions on the aircraft, a time lag exists between the two signals that must be determined and corrected
172 prior to flux calculation.

173 To confirm that the two CPCs sampled identical air masses simultaneously, Spearman correlation coefficients were
174 calculated for concentration measurements from both CPCs after removing cloud shattering artifacts and excluding
175 SPE periods. From the complete campaign dataset, 370 randomly selected seconds of data yielded an average
176 Spearman correlation coefficient of 0.97 (Supplementary Figs. S2–S3), confirming adequate synchronization between
177 the two concentration records. However, a high correlation coefficient alone does not determine the precise temporal
178 offset between the two signals.

179 Lag times between the two CPC signals were determined individually for every 20-second interval (representing the
180 time taken for the airplane to traverse 2 km) using covariance maximization, shifting one CPC relative to the other
181 signal to identify the temporal offset that maximizes their covariance. A single fixed lag time across the entire
182 campaign was not appropriate, given the variability in lag times observed across flight segments (Supplementary Fig.
183 S4). This approach was independently validated using pressure measurements from the isokinetic inlet and static
184 pressure from the AIMMS-20 probe. The two pressure records yielded a Spearman correlation coefficient of 0.99,
185 confirming that both instruments consistently sampled the same air mass with no systematic offset (Supplementary
186 Fig. S6). Similarly, covariance maximization applied to the pressure records confirmed that no single lag time was
187 appropriate across the full campaign (Supplementary Fig. S7), consistent with the CPC-based analysis and further
188 supporting the use of individually determined lag times for each flux calculation period.

189 **2.4 Aerosol number flux calculations**

190 Flux measurement methods were originally developed for tower-based platforms, and their application to aircraft
191 measurements introduces fundamental differences in sampling characteristics that must be carefully considered.
192 Tower measurements provide continuous observations at fixed heights, capturing the complete turbulent eddy
193 spectrum including low-frequency contributions essential for accurate flux estimates (Helbig et al., 2021; Sakai et al.,
194 2001). Aircraft measurements, by contrast, sample different air masses as the platform moves horizontally, effectively
195 trading temporal for spatial averaging (Desjardins et al., 1989)

196 Three interconnected challenges arise specifically for aircraft-based flux measurements. First, turbulent intensity in
197 convective boundary layers increases with height above the surface layer before decreasing above 0.3–0.4 z_i (where z_i
198 is the boundary layer height). Maintaining flux variance within 10% therefore requires measurement lengths of 100
199 to 10^4 times the boundary layer height (Lenschow and Stankov, 1986), a constraint that becomes increasingly difficult
200 to satisfy at the higher altitudes routinely sampled by research aircraft. Second, high aircraft speeds impose strict
201 constraints on sensor response times: for an aircraft traveling at 100 m s^{-1} , a 1 Hz sampling system resolves eddies no
202 smaller than 200 m, approaching the lower limit for capturing the dominant flux-carrying scales. The CPCs used in
203 this study operate at 1 Hz, meaning that contributions from smaller eddies are not resolved and must be accounted for
204 through flux loss corrections (Section 2.8). Third, and most critically for flux calculation, aircraft measurements are
205 inherently non-stationary as the platform continuously moves through different air masses, meteorological conditions,
206 and altitudes. Traditional eddy covariance methods assume stationarity over the averaging period, a condition that is
207 difficult to maintain during aircraft sampling (Gioli et al., 2004).

208 To address this limitation, this study employs the continuous wavelet transform (CWT) method for flux derivation.
 209 The primary advantage of the CWT approach is that it does not require stationarity and eliminates the need for data
 210 detrending, thereby avoiding systematic errors that can arise from linear detrending procedures (Rannik and Vesala,
 211 1999). This study follows CWT flux derivation method of (Torrence and Compo, 1998), described below.

212 The wavelet coefficient, $W_N(a,b)$, for a function $x(z)$ which changes with height, is calculated as a function of both
 213 location (height for airborne measurements or time for ground-based measurements) and scale (frequency or
 214 wavenumber) through convolution with a wavelet function (ψ):

$$215 \quad W_N(a, b) = \int_{-\infty}^{\infty} x(z) \psi_{a,b}(z) dz \quad (1)$$

216 where (z) represents the wavelet function, controlled by the scale parameter (a) and translation parameter (b). The
 217 scale parameter governs the wavelet frequency, while the translation parameter shifts it in the temporal domain. The
 218 wavelet function is defined as:

$$219 \quad \psi_{a,b}(z) = \frac{1}{\sqrt{a}} \psi_0\left(\frac{z-b}{a}\right) \quad (2)$$

220 All wavelet functions are based on a “mother” wavelet, . For this study, the Morlet wavelet is chosen as the mother
 221 wavelet, which is the product of a plane wave with a Gaussian function (Torrence and Compo, 1998). Schaller et al.,
 222 (2017) reported that the Morlet wavelet provides reliable results in flux analysis even when traditional eddy covariance
 223 methods fail.

$$224 \quad \psi_0(\eta) = \pi^{-\frac{1}{4}} e^{i\omega_0\eta} e^{-\frac{\eta^2}{2}} \quad (3)$$

225 where ω_0 is the non-dimensional frequency (set to 6 for this study), and η is the non-dimensional time parameter and
 226 , the first exponential term is the complex sinusoid, and the second exponential term is the Gaussian envelope. Using
 227 this methodology, the vertical turbulent particle flux can be calculated according to (Schaller et al., 2017; Torrence
 228 and Compo, 1998) as:

$$229 \quad \overline{w'(z)N'_{3-10}(z)} = \frac{\delta_t}{C_\delta} \times \frac{\delta_j}{L} \times \sum_{n=0}^{L-1} \sum_{j=0}^J \left[\frac{W_N(a,b) \times W_w^*(a,b)}{a(j)} \right] \quad (4)$$

230 C_δ , the wavelet specific reconstruction factor is taken as 0.776, which is empirically derived for the chosen wavelet
 231 (Schaller et al., 2017; Torrence and Compo, 1998) , L represents the number of elements in the time series with
 232 timestep δ_t which is the inverse of frequency (1 Hz for this study), J is the maximum number of scales with δ_j being
 233 the space between each discrete scale (Schaller et al., 2017; Torrence and Compo, 1998).

$$234 \quad J = \delta_j^{-1} \times \log_2\left(\frac{L \times \delta_t}{s_0}\right) \quad (5)$$

235 δ_j was chosen to be 0.25 s (Schaller et al., 2017; Torrence and Compo, 1998), this value can be adjusted to get better
 236 scale resolution at the expense of higher computational cost, s_0 is the smallest scale of the wavelet taken as $2\delta_i$, $a(j)$ is
 237 the scale parameter for the discrete scale calculated as:

$$238 \quad a(j) = s_0 \times 2^{j\delta_j} \quad j = 0, 1, \dots, J \quad (6)$$

239 $W_N(a,b)$ is the wavelet coefficient for the particle concentration signal, and $W_w^*(a,b)$ is the complex conjugate of the
 240 wavelet coefficient for the vertical velocity signal. Under stationary conditions, fluxes calculated using both CWT and
 241 traditional eddy covariance methods should yield equivalent results, though agreement may vary in aircraft
 242 measurements due to the presence of non-stationarities (Misztal et al., 2014; Wolfe et al., 2018).

243 **2.5 Limit of Detection Determination**

244 Spirig et al., (2005) demonstrated that calculating covariance at time ranges significantly larger than the integral time
 245 scale can quantify the precision of individual flux determinations. The integral time scale was calculated using the
 246 cross-correlation function between vertical wind w and 3-10 nm sized particle size concentration, using the method
 247 described by (Lenschow et al., 2000; Wulfmeyer et al., 2016). The cross covariance is given as:

$$248 \quad A_{x,y}(\tau) = \text{cov}(x_t, y_{t+\tau}) \quad (7)$$

249 Where x_t and y_t are the two signals of interest, with y shifted by the lag time τ . Now the cross covariance is fitted to a
 250 model of the form:

$$251 \quad A_{\text{model}}(\tau) = v - k\tau^{\frac{2}{3}} \quad (8)$$

252 Where v and k are fitted parameters. The line is fitted till the first zero crossing of the cross covariance. And using
 253 this, the integral timescale, I is calculated as:

$$254 \quad I = \frac{2}{5} \left(\frac{v}{k} \right)^{3/2} \quad (9)$$

255 The median value of the integral timescale for the flux events was ~ 11 seconds. The limit of detection (LoD) is
 256 defined as 1.96 times (95% confidence interval) the standard deviation of covariance between w and N_{3-10} when one
 257 of the signals is temporarily shifted with respect to the other. To estimate the precision of an individual flux
 258 determination, we followed Spirig et al. (2005) and examined fluctuation of the covariance function at time lags far
 259 away from the true lag. The standard deviations of the covariance function were calculated between 4500 to 5700
 260 seconds (corresponding to 45 to 57 km spatial displacement) before and after the peak fluxes. These lag times were
 261 selected to be much higher than the integral timescale of turbulence at all measurement heights. . The limit of detection
 262 (LoD) is defined as 1.96 times (95% confidence interval) the standard deviation of covariance between w and N_{3-10}
 263 when one of the signals is temporarily shifted with respect to the other. Signal shifts -10 to $+10$ seconds
 264 (corresponding to ± 1 km spatial displacement) are applied to ensure complete decoupling between the signals. Flux
 265 calculations are restricted to periods when the aircraft maintained horizontal, straight line flight segments to ensure
 266 reliable flux estimates and minimize the influence of aircraft maneuvers on turbulence measurements. The limit of

267 detection is used as an absolute value and hence if a particular flux event is lower in absolute value compared to the
268 LoD, they will not be considered for analysis.

269 **2.6 Small particle events selection criteria**

270 Establishing appropriate threshold values for new particle formation over tropical oceanic regions presents significant
271 challenges due to sparse observational datasets and the intricate interactions between meteorological and chemical
272 processes in these environments. Earlier studies have typically used concentration thresholds of 10^3 to 10^4 particles
273 cm^{-3} for ultrafine particles (3–25 nm) to distinguish nucleation events from background conditions. However, these
274 criteria were primarily established based on observations from continental or mid-latitude marine environments (Dal
275 Maso et al., 2005; Kulmala et al., 2012). Given that tropical marine regions are characterized by reduced background
276 aerosol loadings and distinct precursor gas profiles relative to higher latitude zones, more conservative thresholds
277 (500 – 1000 particles cm^{-3}) may prove better suited for detecting nucleation phenomena in these relatively unpolluted
278 environments (Modini et al., 2009; Weber et al., 1997). Additionally, the aircraft-based measurement method
279 prevented the implementation of traditional nucleation event identification criteria, specifically the requirement for
280 persistent concentration increases spanning 1–2 hours to distinguish genuine nucleation from brief local source
281 influences (Kulmala et al., 2012).

282 For this study, we modified the methodology established by Zheng et al., (2021) to detect small particle
283 events (SPEs). Individual 1-second measurements were used to identify when N_{3-10} concentrations exceeded 150 cm^{-3} ,
284 once identified the measurements that exceeded the threshold were grouped into 10-second intervals (equivalent to ~ 1
285 km spatial resolution), and the average N_{3-10} for the group was checked to see if it achieved statistical significance
286 using:

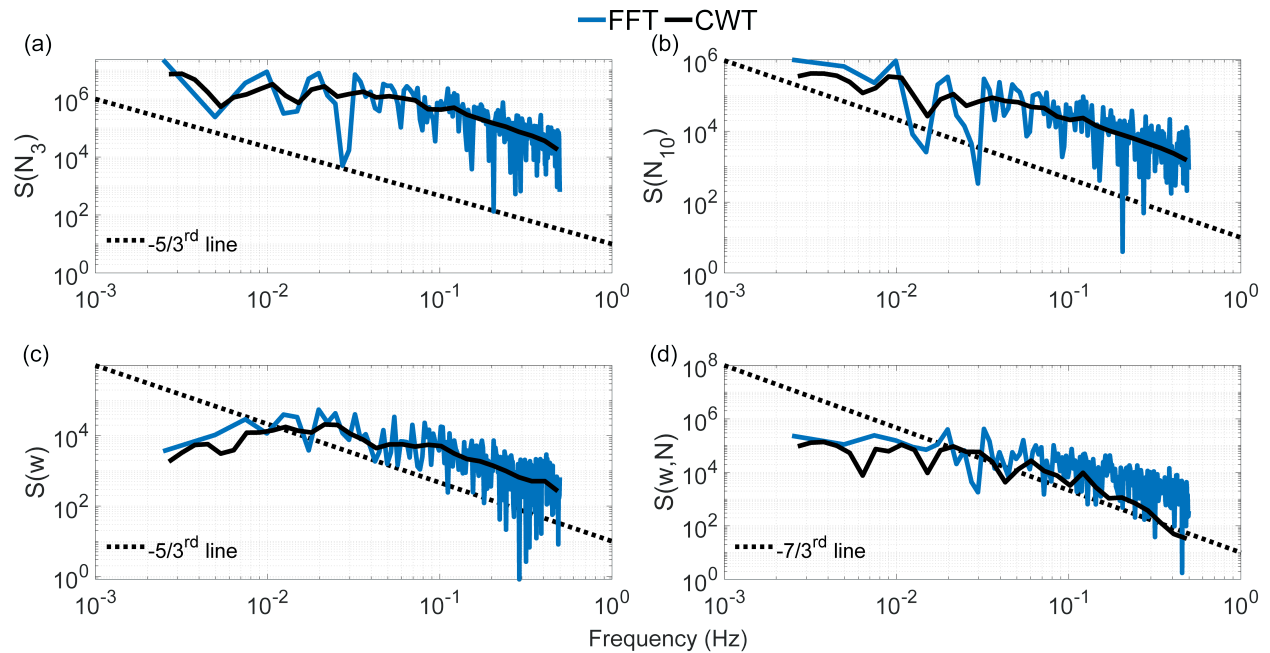
$$287 \quad N_3 - N_{10} > 3\sigma_D \quad (10)$$

288 where σ_D represents the uncertainty in the concentration difference between N_3 and N_{10} , expressed as:

$$289 \quad \sigma_D = \sigma(N_3 - N_{10}) \quad (11)$$

290 **2.7 Frequency response and flux averaging time**

291 Momentum, enthalpy, and matter are transported in the atmosphere by eddies of different spatial scales. One-
292 dimensional power spectral analysis is used to decompose the signal into components of different frequencies, which
293 are associated with different eddy sizes. Fast Fourier Transform (FFT) and Continuous Wavelet Transform (CWT)
294 were used to calculate the power spectral density (PSD) of vertical wind speed and particle concentration.



295

296 **Figure 1. Power spectral density for (a) N_3 , (b) N_{10} , (c) vertical wind velocity, and (d) 3-10 nm particle flux.**

297 Figure 1 shows the PSD for a flight leg on 21 June 2017 between 13:43 and 13:49 UTC at a height of 550 m above
 298 mean sea level. Dashed lines represent the theoretical slopes for the inertial subrange, which describe how energy
 299 cascades from larger to smaller eddies and finally dissipates as heat due to viscous friction (Pope, 2000). Both particle
 300 concentration spectra (Figs. 1a,b) and the flux spectrum (Fig. 1d) broadly follow the theoretical $-5/3$ and $-7/3$
 301 Kolmogorov scaling across the resolved frequency range. The supplementary figure comparing 1 Hz and 10 Hz
 302 vertical wind velocity spectra (Supplementary Fig. S8) confirms that turbulent energy exists at scales beyond the 1 Hz
 303 Nyquist frequency. The absence of a visible noise floor in the particle concentration spectra at high frequencies reflects
 304 the band-limited response of the CPC, which acts as a low-pass filter that attenuates high-frequency concentration
 305 fluctuations, producing a steep spectral roll-off rather than a white noise floor. While this results in a cleaner spectrum
 306 visually, it still represents real flux loss at high frequencies that is accounted for through the correction described in
 307 Section 2.8.

308

309 Figure 1 also shows some differences between FFT and CWT flux calculations, especially for fluxes at high
 310 frequencies. These differences are attributable primarily to non-stationarity in the aircraft data, as the platform moves
 311 through different air masses, meteorological conditions, and altitudes. FFT assumes stationarity over the entire
 312 analysis window and can therefore introduce artifacts under such conditions, whereas CWT provides time-localized
 313 frequency information that is more robust for non-stationary signals (Schaller et al., 2017). Li et al., (2023) evaluated
 314 uncertainties of turbulent flux calculation using both methods, finding that biases can range from 50–100% of the
 315 spectrally complete flux. We note that the high-frequency deviations visible in the particle concentration spectra are
 316 not a consequence of FFT limitations but reflect the band-limited response of the CPC, which attenuates concentration

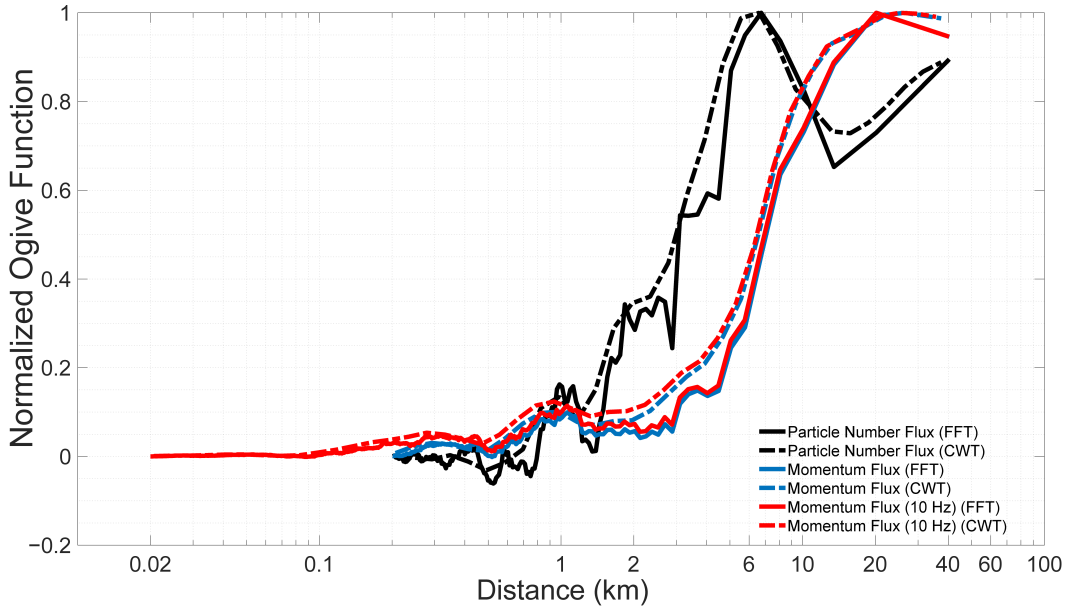
317 fluctuations at frequencies above ~ 0.3 Hz, as discussed in Section 2.8. The CWT's more conservative high-frequency
318 response may better represent the actual resolvable flux contributions (Misztal et al., 2014).

319 To assess whether the calculated fluxes adequately represent both low- and high-frequency turbulent contributions,
320 we conducted ogive analysis using the approach described by Foken et al., (2006). Mobile measurement platforms
321 necessitate modified considerations for flux averaging intervals. Standard 30-minute averaging periods used in
322 stationary tower observations are inappropriate for aircraft measurements. Considering the aircraft's ground speed, a
323 90-second sampling period covers an equivalent air mass to that sampled by a stationary sensor over 30 minutes at
324 typical wind speeds of 5 m s^{-1} . To enable direct comparison between ogives computed using FFT and CWT methods,
325 normalization was applied according to Sun et al., (2018):

$$326 \quad \widehat{og}(f) = \frac{og(f)}{sgn\{\max(og(f)) + \min(og(f))\} \max(|og(k)|)} \quad (12)$$

327 where $sgn\{x\}$ represents the signum function, returning +1 for positive x , -1 for negative x , and zero when x equals
328 zero. When the normalized ogive equals 1, the ogive value corresponds precisely to the covariance value for that
329 averaging period. The advantage of this normalization approach is that it facilitates the identification of cases where
330 low-frequency turbulence has an opposite sign to high-frequency turbulence. In such situations, large and small eddies
331 transport material in opposing directions, indicating complex atmospheric processes such as counter-gradient
332 transport. The normalized ogive plot visually reveals these opposing contributions through characteristic rise-and-fall
333 patterns that might otherwise be obscured in non-normalized data.

334 Figure 2 illustrates the ogive as a function of distance covered by the aircraft for the same flight leg shown in Fig. 1.
335 Signal frequency was converted to distance by dividing the aircraft speed (assumed to be constant at 100 m s^{-1}) by the
336 frequency obtained from the FFT or CWT analysis. This plot reveals that the particle flux for this flight leg can be
337 resolved by averaging over 40 km. While both FFT and CWT ogives show agreement for this case, such consistency
338 cannot be expected universally; therefore, CWT fluxes are used throughout this study for the reasons discussed in
339 previous sections.



340

341 **Figure 2: Normalized ogive function as a function of distance covered by the aircraft. The ogive represents the cumulative**
 342 **fractional contribution to total flux from high to low frequencies.**

343 2.8 Flux loss correction

344 If the sensor used to measure fluxes are too slow to accurately capture the smaller eddies that contribute to the total
 345 flux, the turbulent fluxes will require correction. For micrometeorological flux measurements on towers at 10 m above
 346 the surface, instruments are typically operated at 10 Hz (Nyquist frequency = 5 Hz). Under typical wind speeds of 5
 347 m s^{-1} , this sampling rate can resolve eddies as small as ~ 1 m, ensuring that most energy-containing and inertial
 348 subrange eddies are captured (Aubinet et al., 2012; Lee et al., 2005; Stull, 1988).

349 However, airborne flux measurements present different challenges. The integral length scales of turbulent eddies
 350 increase approximately linearly with height within the surface layer (roughly the bottom 10% of the boundary layer),
 351 then remain approximately constant above this level, limited by the boundary layer height (Kaimal and Finnigan,
 352 1994). In the mixed layer portion of a typical boundary layer (above ~ 100 m surface layer), integral length scales are
 353 typically 100-200 m (Lenschow and Stankov, 1986). At an aircraft ground speed of 100 m s^{-1} , the 1 Hz sampling
 354 provides 200 m spatial resolution, which approaches but does not fully resolve the integral length scale. Consequently,
 355 the sampling resolution approaches the lower limit for adequately resolving the dominant flux-carrying scales and
 356 may under sample contributions from smaller turbulent structures.

357 To address this limitation, we applied the approximations from Horst (1997) to estimate the ratio of measured flux
 358 (F_m) to spectrally complete flux (F) for different atmospheric stability conditions encountered during campaign flights:

$$359 \frac{F_m}{F} = \frac{1}{1 + (2\pi n_m \tau_c \frac{\bar{u}}{z})^\alpha} \quad (13)$$

360 where F_m is the measured flux, F is the spectrally complete flux, \bar{u} is the magnitude of average wind speed, z is the
 361 height of the airplane, τ_c is the response time constant of the CPC, which was taken as 3.0 s, $\alpha = \text{seven-eighths-}$ and n_m

362 = 0.085 for neutral and unstable conditions (Pryor et al., 2007). Equation 13 was originally developed by Horst (1997)
363 to estimate the attenuation of scalar flux measurements within the surface layer, but has been applied to aircraft
364 measurements (Gioli et al., 2004), with corrected airborne fluxes showing good agreement with tower data when
365 aircraft measurements were conducted over homogeneous surfaces at altitudes comparable to tower height.
366 To illustrate the practical importance of this correction, the $\frac{F_m}{F}$ ratio varies substantially depending on measurement
367 height and atmospheric stability conditions encountered during the campaign. For measurements conducted near the
368 top of the marine boundary layer (~1,200–1,400 m) under near-neutral to unstable conditions, $\frac{F_m}{F}$ values approach
369 unity (0.93–0.99), indicating that flux losses are modest at these heights where the dominant flux-carrying eddies are
370 large relative to the CPC response limitation. However, for measurements conducted closer to the surface (~30–550
371 m), $\frac{F_m}{F}$ values range from 0.70 to 0.95, implying that uncorrected fluxes could underestimate the spectrally complete
372 flux by up to 30%. This highlights the importance of applying the flux loss correction, particularly for low-altitude
373 flight legs where eddy sizes are smaller and the CPC response time constant becomes a more significant fraction of
374 the dominant flux-carrying eddy turnover times.
375 Following the approach of (Islam et al., 2022), we assessed the random uncertainty in particle flux due to counting
376 statistics. We found it to be 2–3 orders of magnitude lower compared to the measured flux magnitudes reported in this
377 study. Therefore, the correction due to discrete counting statistics of CPCs was not applied to this study.

378 **3.0 Results**

379 We examine two flight days as case studies of SPEs observed at varying altitudes above the ocean. Additional
380 supporting flights are presented in the Supplementary Information. Table 1 summarizes the N_{3-10} vertical turbulent
381 flux estimates derived from all six flight days analyzed in this study, grouped by the inferred nucleation regime. Flights
382 1 and 2 (January 29 and February 10, 2018) are classified as entrainment zone nucleation events, where SPEs were
383 detected near the top of the MBL at heights exceeding 1,200 m. Flights 3–6 (June 21 and July 7, 2017; February 18
384 and 12, 2018) are classified as decoupled layer nucleation events, with SPEs observed across a broader range of
385 altitudes (30–837 m). For all events, the ratio of measured flux to the spectrally complete flux ($\frac{F_m}{F}$) exceeds 0.76,
386 indicating minimal flux loss due to sensor response limitations. The normalized vertical velocity variance ($\sigma_w^2 w_*^{-2}$)
387 is generally low, consistent with relatively quiescent turbulent conditions during the measurement periods. Negative
388 flux values indicate downward transport of freshly nucleated particles from the entrainment zone toward the surface,
389 while positive values suggest upward transport from a source within the decoupled sub-cloud layer. Two of these
390 flight days, January 29, 2018 (Case 1) and June 21, 2017 (Case 2), are examined in detail as case studies in the
391 following sections, with the remaining four flights presented as supporting examples in the Supplementary
392 Information.

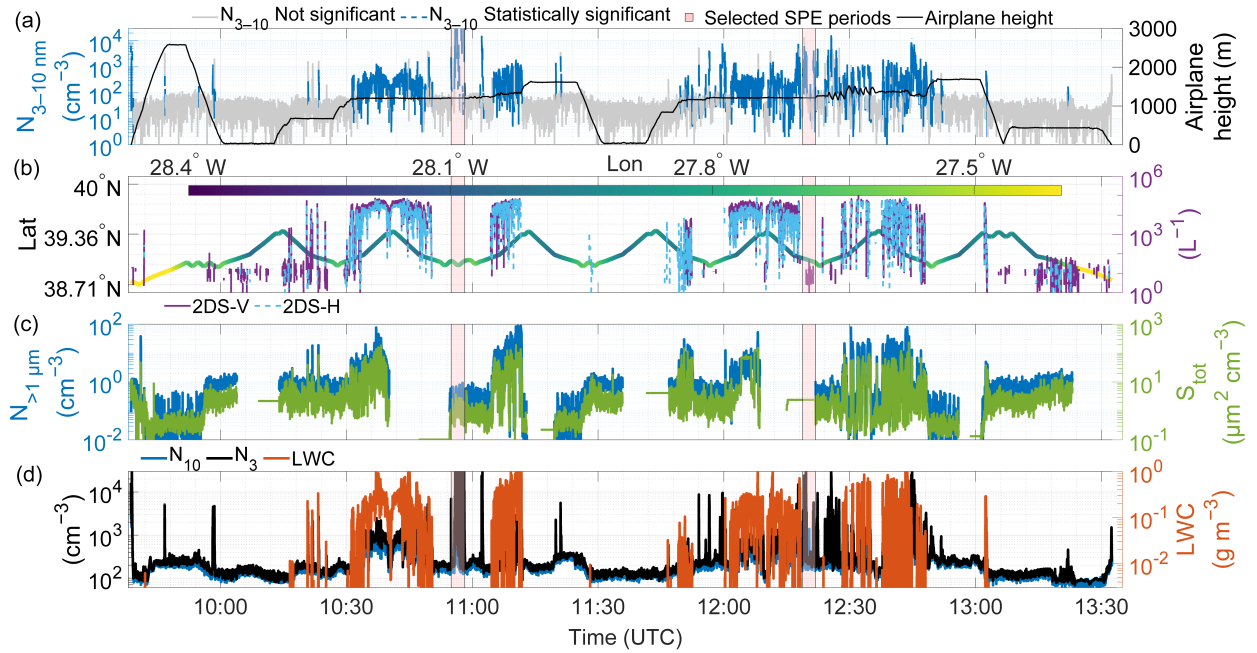
393 Table 1. Summary of N_{3-10} particle vertical turbulent flux estimates from aircraft campaigns with detection limits and
394 flux loss assessment.

No	Date	Time (UTC)	Height (m)	N_{3-10} flux ($\text{cm}^{-2} \text{s}^{-1}$)	LoD ($\text{cm}^{-2} \text{s}^{-1}$)	F_m/F	$\sigma^2 w_*^{-2}$
Entrainment zone nucleation							
1	01/29/18	10:54:59-10:58:13	1,205	-41,092	34,423	0.97	0.01
		12:18:47-12:21:50	1,218	-2,975	2,085	0.98	0.005
2	02/10/18	13:53:20-13:55:02	1,375	-1,195	381	0.93	0.003
Decoupled layer nucleation							
3	06/21/17	14:03:30-14:09:25	800	1,139	294	0.99	0.016
		13:56:10-14:02:25	800	2,929	1,239	0.98	0.021
		13:42:40-13:49:23	550	-2,782	1,995	0.95	0.1
		13:32:20-13:38:40	30	-860	400	0.76	0.17
4	07/07/17	13:42:18-13:43:04	565	-94,093	49,410	0.86	0.02

		13:43:07-13:44:58	535	-21,317	4,959	0.90	0.031
5	02/18/18	14:17:32-14:19:38	555	298	115	0.81	0.016
		14:47:10-14:51:34	250	-3,217	1,153	0.70	0.056
6	02/12/18	14:54:27-14:58:37	837	5,433	1,173	0.93	0.04

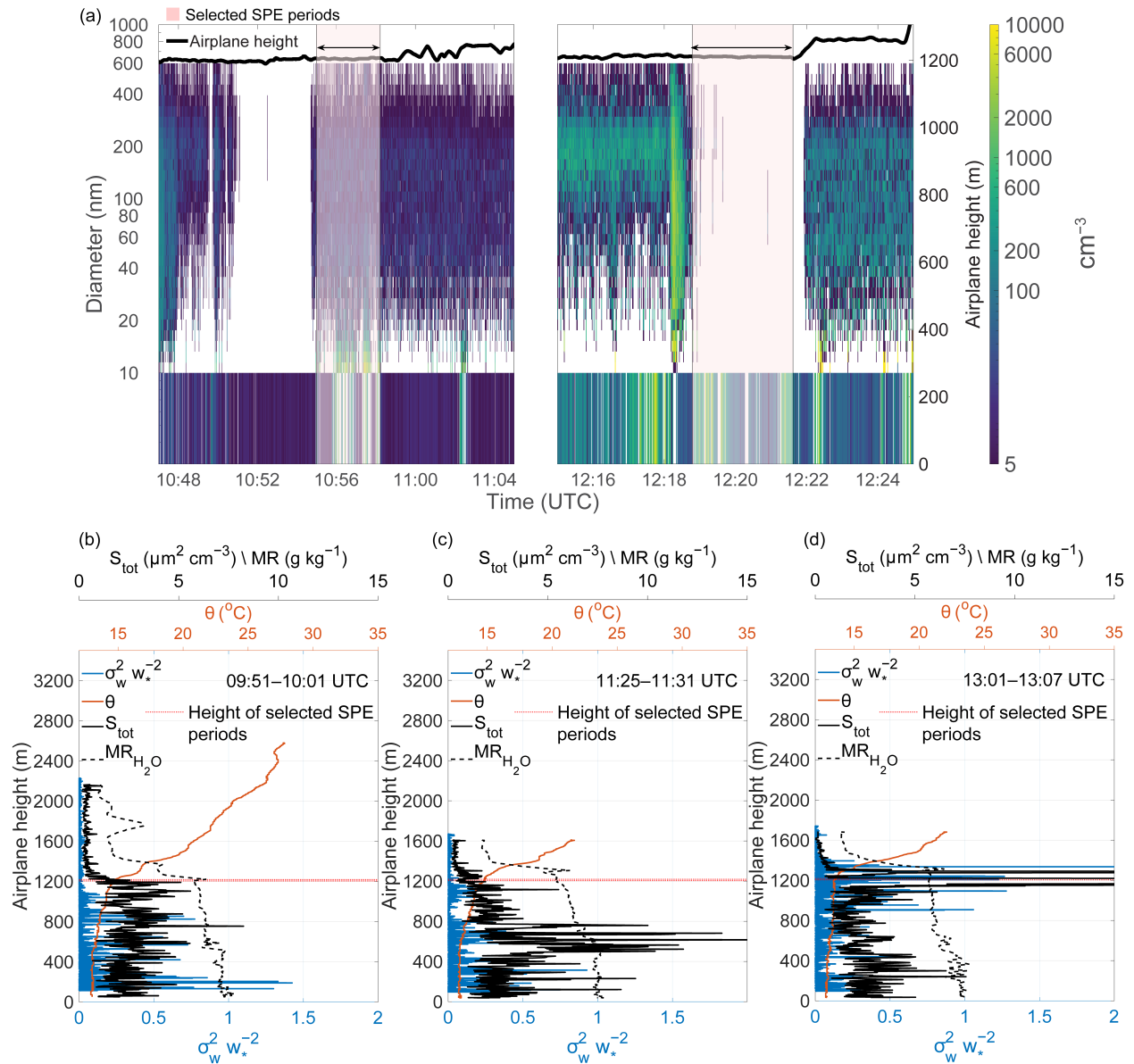
395 **Case 1: SPE occurring in the entrainment zone near the top of the marine boundary layer**

396 Figures 3–5 present data collected on January 29, 2018 with an additional example from February 10, 2018, shown in
397 Supplementary Figs. S9–S11. Back-trajectory analysis (not shown) indicates that the sampled airmasses had been
398 circulating around the Azores for the preceding three days and were therefore likely less polluted than North American
399 outflow air masses. Figure 3 shows a multi-panel time series covering approximately 3.5 hours of flight operations.
400 The aircraft initially ascended to ~2,500 m but generally remained below ~1,500 m for most of the flight (Fig. 3a).
401 The flight trajectory (Fig. 3b) reflects predominantly east-west movement across the Azores region, spanning latitudes
402 from approximately 38.7° to 39.4°N and longitudes from -28.4° to -27.4°W. Drizzle number concentration measured
403 by 2DS (purple and blue lines in Fig. 3b) was absent or low during the selected SPE periods. Elevated drizzle number
404 concentration, together with high liquid water content regions (orange in Fig. 3d), mark frequent cloud encounters.
405 Following our quality control procedures, all N_{3-10} concentration data with $LWC \geq 3 \times 10^{-3} \text{ g m}^{-3}$ were excluded from
406 analysis to avoid contamination from cloud droplet shattering artifacts. Pink-shaded periods mark the intervals chosen
407 for detailed analysis, which exhibited simultaneous increases in both N_3 and N_{10} concentrations exceeding 10^4 cm^{-3}
408 (indicating an SPE). Supermicron particle concentration (blue in Fig. 3c) as well as total particle surface area (green
409 in Fig. 3c) were also low during the selected SPE periods, indicating the absence of particles such as sea spray aerosols.
410



411

412 **Figure 3. Multi-parameter time series from the January 29, 2018 flight. (a) N_{3-10} particle concentrations and aircraft**
 413 **altitude; (b) aircraft position (latitude and longitude) and drizzle number concentration; (c) supermicron particle**
 414 **concentration and total particle surface area (S_{tot}); (d) particle number concentrations (N_{10} and N_3) and liquid water**
 415 **content. Gaps in the time series indicate the missing data.**



416

417 **Figure 4. (a) Size-resolved particle number concentrations (10–600 nm) from FIMS as a function of time and altitude, with**
 418 **N_{3-10} concentrations shown in the lower strip. Pink shading indicates selected SPE periods. (b–d) Vertical profiles of**
 419 **potential temperature (θ), normalized vertical velocity variance ($\sigma_w^2 w_*^{-2}$), total particle surface area (S_{tot}), and water vapor**
 420 **mixing ratio ($\text{MR}_{\text{H}_2\text{O}}$) for three time periods nearest to the selected SPE periods: (b) 09:51–10:01 UTC, (c) 11:25–11:31**
 421 **UTC, and (d) 13:01–13:07 UTC. Gaps in the time series indicate the missing data.**

422

423 Figure 4a shows the temporal evolution of particle concentration between $\sim 10:47$ – $11:05$ and $\sim 12:15$ – $12:25$ UTC. The
 424 colormap represents FIMS-derived, size-resolved aerosol number concentrations (10–600 nm diameter), varying
 425 across time and altitude, while the lower panel displays N_{3-10} concentrations. The two pink-highlighted intervals are
 426 the same as in Fig. 3. The high particle concentration spike observed $\sim 12:18$ UTC coincides with elevated LWC and
 427 drizzle concentration (Fig. 3d) and was excluded from analysis following our quality control procedures (Section
 428 2.3.1). Weber et al. (1998) documented that cloud droplet shattering can produce artificial particle concentrations as

429 small as 3 nm in airborne CPC measurements, making this the most plausible explanation for the observed spike.
430 Aircraft exhaust contamination can be ruled out, as the nearest prior flight transect over this region occurred
431 approximately half an hour earlier at an altitude ~ 60 m lower, more than sufficient time and vertical separation for
432 complete plume dispersal. This data point was therefore excluded from all flux calculations as the concurrent LWC
433 exceeded the quality control threshold of 3×10^{-3} g m $^{-3}$.

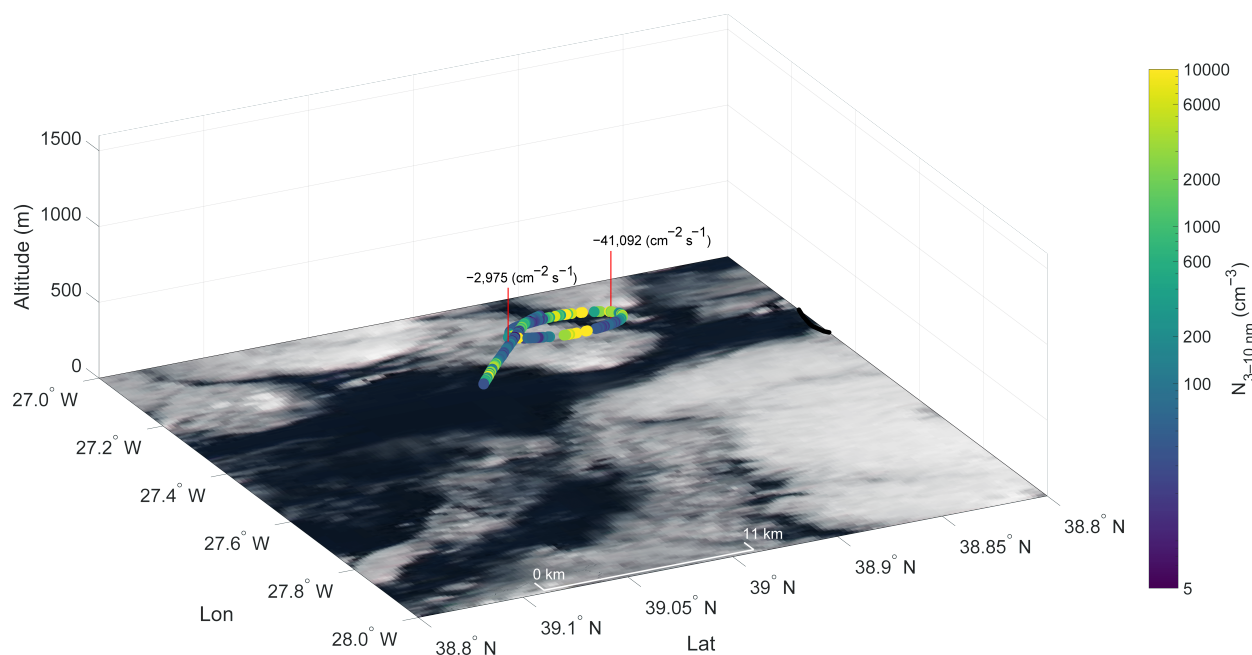
434 Figures 4b–d present vertical profiles of potential temperature, normalized vertical velocity variance ($\sigma_w^2 w_*^{-2}$) i.e.,
435 (the vertical velocity variance normalized by the square of the convective velocity scale), total particle surface area,
436 and the water vapor mixing ratio at three locations nearest to the pink-highlighted intervals. Sharp gradients in the
437 potential temperature (orange) mark the top of the MBL, defining the capping inversion that suppresses vertical mixing
438 between the boundary layer and the free troposphere. The co-occurrence of these temperature gradients with elevated
439 normalized vertical velocity variance ($\sigma_w^2 w_*^{-2}$) near the inversion level indicates the presence of an entrainment zone,
440 where thermodynamic forcing (including cloud-top radiative cooling and wind shear) drives mixing between the free
441 tropospheric air above and the convective boundary layer below (Boers and Eloranta, 1986)). Figures 4b–d reveal a
442 deep boundary layer with the entrainment zone between approximately 1,200–1,400 m, consistent with previous
443 estimates that entrainment zones typically comprise 20–40% of boundary layer depth (Martin et al., 2014).

444 Figures 4b–d present the profiles of ($\sigma_w^2 w_*^{-2}$) profiles, a metric that characterizes the intensity of turbulent structures
445 in convective boundary layers (Deardorff, 1974; Dewani et al., 2023). These profiles show elevated ($\sigma_w^2 w_*^{-2}$) values
446 near the ocean surface and within the entrainment zone, with minimal values in the free troposphere, where significant
447 turbulence is absent.

448 The water vapor mixing ratio profiles in Figs. 4b–d reveal evolving boundary layer moisture structure during the
449 flight. The early profile (Fig. 4b) shows a relatively well-mixed moisture distribution below the capping inversion at
450 $\sim 1,200$ m, with a sharp decrease into the drier free troposphere above. The latter profiles (Figs. 4c–d) exhibit a two-
451 step moisture structure, with a sharper gradient near ~ 600 m suggesting progressive decoupling of the boundary layer
452 during the course of the flight, separating a moister surface layer from a drier sub-cloud layer above. Despite some
453 vertical variability shown in Figs. 4b–d, the total particle surface area (S_{tot}) remained relatively low throughout the
454 flight, falling well below the campaign averages of ~ 30 $\mu\text{m}^2 \text{cm}^{-3}$ in the surface mixed layer and ~ 10 $\mu\text{m}^2 \text{cm}^{-3}$ in the
455 upper decoupled layer reported by Zheng et al. (2021). Figure 4c also shows a distinct S_{tot} maximum at an altitude
456 where small gradients in both potential temperature and mixing ratio suggest the presence of an entrainment layer.
457 The pronounced S_{tot} increase could indicate a nucleation occurring at this location (see Case 2 below), although this
458 hypothesis could not be independently verified looking at the N_{3-10} data in this case. Figure 4c shows that the
459 entrainment zone and free troposphere were characterized with extremely low S_{tot} values.

460 Figure 5 presents the spatial distribution of N_{3-10} particle concentrations along the flight path at $\sim 1,200$ m altitude
461 (dashed lines in Figs. 4b–d), with the calculated vertical turbulent fluxes labeled at their respective measurement
462 locations. Concentrations up to $10,000 \text{ cm}^{-3}$ were observed along the flight track, with the highest values concentrated
463 within a horizontal extent of less than 10 km. The substantial downward fluxes of N_{3-10} particles ($-41,092$ and $-2,975$
464 $\text{cm}^{-2} \text{ s}^{-1}$) at $\sim 1,200$ m both exceed their respective limits of detection (Table 1), confirming that the observed downward
465 transport represents a statistically significant atmospheric signal rather than measurement noise. The downward flux

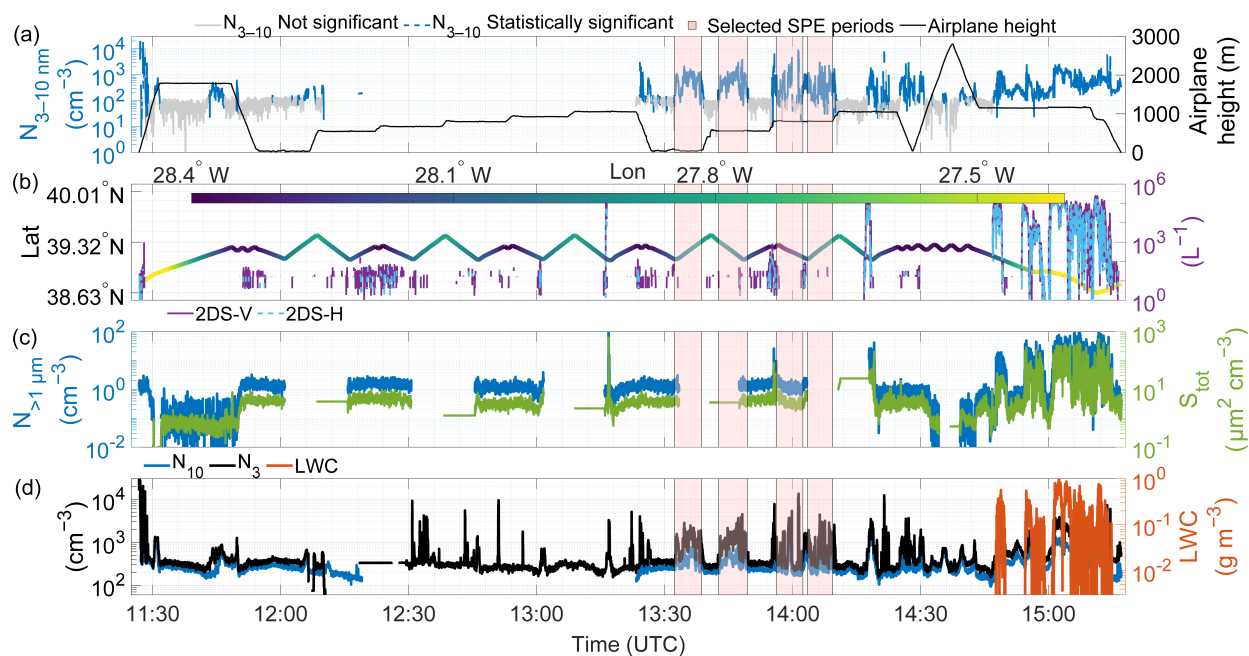
466 direction indicates that the source of freshly nucleated particles was located above the measurement altitude, within
 467 the entrainment zone, while the large difference in flux magnitudes between the two events likely reflects spatial
 468 heterogeneity in source strength and the proximity of the aircraft to the nucleation zone during each transect. This
 469 interpretation is supported by the near-absence of N_{3-10} at $\sim 1,600$ m during 11:14–11:25 and 12:51–13:01 UTC (Fig.
 470 3), with the exception of brief concentration spikes of uncertain origin retained in the record due to insufficient
 471 evidence for their removal. The small particle size (3–10 nm) and limited horizontal extent of less than 10 km further
 472 argue against a free tropospheric nucleation source, as particles originating in the free troposphere would be expected
 473 to have grown substantially and the plume to have diluted during descent to measurement altitude. Several mechanisms
 474 could promote nucleation specifically within the entrainment zone adiabatic cooling in the rising convective plumes,
 475 turbulent fluctuation in temperature and vapor concentration generated by entrainment, and dilution of mixed-layer
 476 air by the entrained free tropospheric air, causing a sudden reduction in preexisting aerosol surface area (Nilsson et
 477 al., 2001). The extremely low S_{tot} values observed in the entrainment zone and free troposphere (Fig. 4), falling well
 478 below the campaign averages, are consistent with this interpretation. These conditions are analogous to those identified
 479 in previous studies linking entrainment zone nucleation to reduced condensation sink environments (Größ et al., 2018;
 480 Meskhidze et al., 2019; Nilsson et al., 2001). Supplementary Figs. S10 and S11 provide additional support, showing
 481 a downward flux of N_{3-10} particles ($-1,195 \text{ cm}^{-2} \text{ s}^{-1}$) at 1,375 m with complete absence of N_{3-10} above $\sim 1,400$ meters,
 482 consistent with SPE occurrence specifically within the entrainment zone between 1,375–1,400 m.
 483 Figures 3–5 and the flux analysis (Table 1) demonstrate that the entrainment zone nucleation near the MBL top
 484 occurred on two days (January 29 and February 10, 2018), representing nearly 5% of flight days. Despite a relatively
 485 small horizontal extent (<10 km), these newly formed particles can be entrained in the boundary layer via vertical
 486 turbulent processes, potentially playing an important role in marine aerosol number budget and, given sufficient time
 487 for growth to CCN-relevant sizes, potentially influencing cloud condensation nuclei concentrations for marine
 488 stratocumulus clouds.



490 **Figure 5. Spatial distribution of N_{3-10} particle concentrations along the flight track at ~1,200 m altitude during the period**
 491 **highlighted in Figures 3 and 4. Calculated vertical turbulent fluxes are labeled at their respective measurement locations.**
 492 **Color scale indicates N_{3-10} particle number concentrations (cm^{-3}). The background shows a true-color satellite-corrected**
 493 **reflectance image from the overpass at 15:15 UTC, with the ocean surface appearing dark and clouds appearing white.**
 494 **Credit: NASA Worldview Snapshots.**

495 **Case 2: SPE occurring at the interface between the well-mixed surface layer and the decoupled layer**

496 Figures 6–8 present data from June 21, 2017, with additional examples from July 7, 2017, February 18, 2018 and
 497 February 12, 2018, shown in Supplementary Figs. S12–S14, S15–17, and S18–S20. Back-trajectory analysis (not
 498 shown) indicates that the sampled air masses originated from the Arctic and were therefore expected to be relatively
 499 clean. Figure 6 covers approximately 4 hours of flight operations, during which the aircraft initially flew at very low
 500 altitudes (~30 and 50 m) near 12:00 and 13:30 UTC before gradually ascending to ~1,000 m. Drizzle number
 501 concentration by 2DS (purple and blue lines in Fig. 6b) was absent or below the threshold during the selected SPE
 502 periods. Multiple events with N_{3-10} concentrations from 10^2 to 10^4 cm^{-3} were observed throughout the second half of
 503 the flight. The flight trajectory (Fig. 6b) reflects predominantly east-west movement, spanning latitudes from
 504 approximately 38.6° to 39.3°N and longitudes from -28.4° to -27.4°W . Pink-highlighted intervals show periods with
 505 concurrent increases in N_3 and N_{10} concentrations exceeding 10^3 cm^{-3} , indicative occurrences of SPEs. As in Case 1,
 506 supermicron particle concentrations (blue in Fig. 6c) and total particle surface area (green in Fig. 6c) remained low
 507 during the selected SPE periods, indicating the absence of coarse-mode particles such as sea spray.

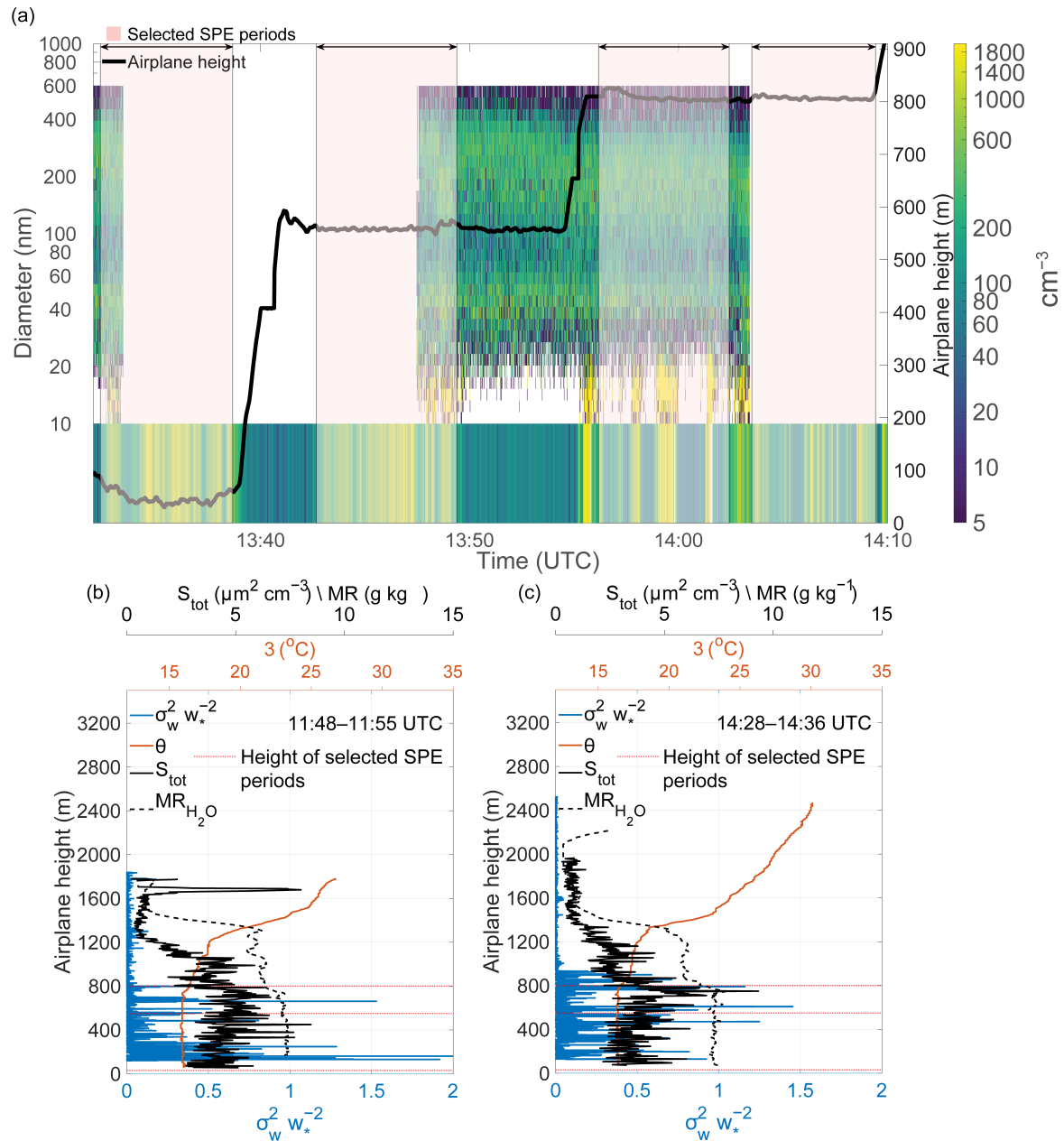


508
 509 **Figure 6. Same as Figure 3 but for June 21, 2017. Gaps in the time series indicate the missing data.**

510 Figure 7a shows size-resolved particle number concentrations evolution during 13:30–14:20 UTC, encompassing the
 511 four pink-highlighted intervals from Fig. 6. The panel Fig. 7a displays N_{3-10} particle concentrations. High N_{3-10}
 512 concentrations were encountered at multiple altitudes, with maximum values exceeding $1,800 \text{ cm}^{-3}$ at ~800 m.

513 The potential temperature and water vapor profiles (Figs. 7b,c) show the MBL structure consisting of a well mixed
514 surface layer extending to ~ 700 m and a decoupled upper boundary layer between ~ 700 –1300 m. Decoupled
515 structures typically form from radiative heating of the cloud layer and evaporative cooling in the sub-cloud layer,
516 which stabilize the boundary layer and suppress vertical mixing (Galewsky et al., 2022; Jones et al., 2011; Wood and
517 Bretherton, 2004). Sharp gradients in both potential temperature and mixing ratio around 1,300 m marking the
518 entrainment zone, above which the free troposphere begins above 1,400 m. The $(\sigma_w^2 w_*^{-2})$ profiles show higher
519 magnitudes in the mixed layer (indicating active turbulence) and low magnitudes in both the decoupled layer (due to
520 stratification and suppressed vertical mixing) and free troposphere. Total particle surface area remained low in the
521 mixed layer but increased considerably toward the top of the mixed layer before decreasing in the decoupled layer and
522 reaching very low values in the free troposphere.

523



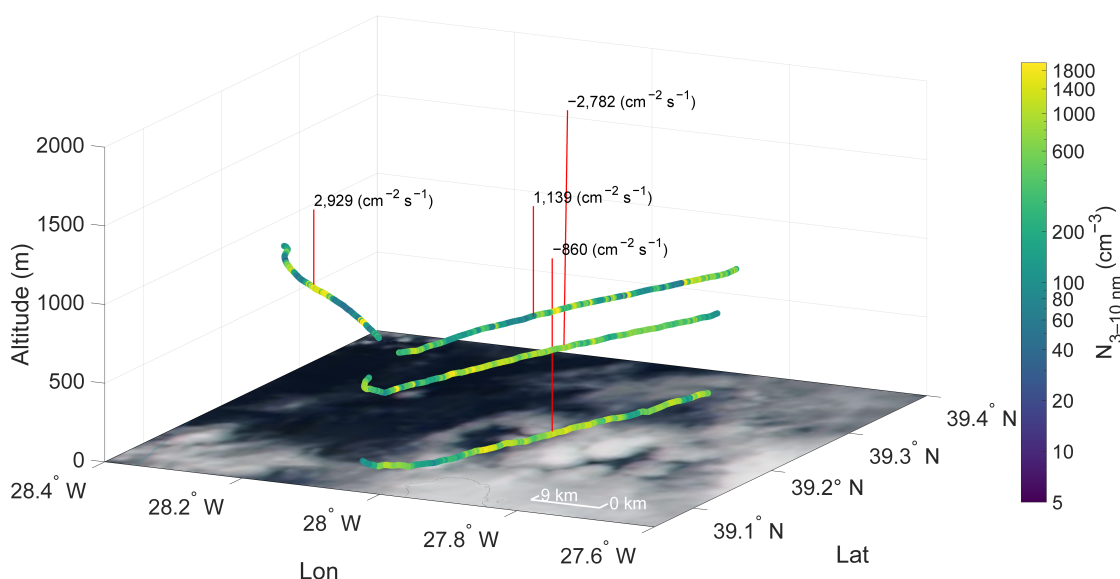
524
525 **Figure 7. Same as Figure 4, but for June 21, 2017. Gaps in the time series indicate the missing data**

526

527 Figure 8 shows N_{3-10} particle concentrations along flight paths at varying altitudes: 30 m, 550 m, and two segments at
528 800 m. We separated the 800 m path to prevent the airplane sampling the same airmass because from 13:55–14:03
529 UTC the aircraft flew along the prevailing wind direction, then changed direction by 90° to fly perpendicular to the
530 wind. The positive vertical turbulent fluxes at 800 and negative values below suggest the SPE occurred between 550–
531 800 meters, likely at the top of the well mixed layer or the bottom of the decoupled layer.

532 The nucleation processes in the entrainment zone and at the base of the decoupled layer could be mechanically
533 similar. Both locations feature the convergence of distinct air masses, in this case, the well-mixed surface layer and

534 the stratified decoupled layer above, which generates turbulent mixing and aerosol dilution effects. While less
 535 pronounced than at the boundary layer top, the interface between these layers exhibits comparable thermodynamic
 536 conditions: potential temperature gradients, contrasting vapor concentrations, and localized adiabatic cooling. Figure
 537 7 demonstrates that the decoupled layer maintains significantly lower aerosol surface area concentrations relative to
 538 the well-mixed layer below, establishing conducive conditions for nucleation when air mass mixing occurs. A key
 539 distinction, however, lies in the spatial characteristics, whereas entrainment zone nucleation showed limited horizontal
 540 extent (<10 km), the decoupled layer event spanned at least 50–60 km, suggesting either more persistent favorable
 541 conditions or a fundamentally different source mechanism operating over regional scales.



542
 543 **Figure 8. Spatial distribution of N_{3-10} particle concentrations along the flight track at varying altitudes (30 m, 550 m, and**
 544 **800 m) during the period highlighted in Figures 6 and 7. Calculated vertical turbulent fluxes are labeled at their respective**
 545 **measurement locations. Color scale indicates N_{3-10} particle number concentrations (cm^{-3}). The background shows a true-**
 546 **color satellite reflectance image from the overpass at 14:15 UTC, with the ocean surface appearing dark and clouds**
 547 **appearing white. Credit: NASA Worldview Snapshots.**

548 Figure 8 reveals a strong negative flux of N_{3-10} ($-2,782 \text{ cm}^{-2} \text{ s}^{-1}$) at 550 m that is nearly three times greater
 549 in magnitude than the flux at 50 m ($-860 \text{ cm}^{-2} \text{ s}^{-1}$), likely due to particle evolution through growth and coagulation,
 550 and dilution processes during vertical transport. The positive fluxes of N_{3-10} observed at 800 m ($2,929$ and $1,139 \text{ cm}^{-2}$
 551 s^{-1}) suggest that nucleation initiated either at the top of the well-mixed boundary layer or at the bottom of the overlying
 552 decoupled layer. This bidirectional flux structure suggests that newly formed particles were transported both upward
 553 and downward from the formation zone through turbulent mixing. The comprehensive analysis presented in Figs. 6–
 554 8, combined with the flux calculations in Table 1, provides some evidence that SPEs can originate within decoupled
 555 layer structures, constituting a significant source of secondary marine aerosols in stratified boundary layer conditions.

556 4. Discussion

557 This study demonstrates the value of vertical turbulent flux measurements for characterizing small particle events
558 (SPE) in remote marine boundary layers. By deriving 3–10 nm particle fluxes from aircraft measurements during the
559 ACE-ENA campaign, we identified two mechanistically distinct SPE scenarios that challenge conventional
560 understanding of marine aerosol sources. Critically, while flux sign alone identifies the vertical location of the particle
561 source, flux magnitude serves two additional essential roles: first, it must exceed the limit of detection to confirm that
562 the observed directional transport represents a statistically significant atmospheric signal rather than measurement
563 noise; and second, it provides quantitative constraints on source strength that cannot be obtained from sign alone.

564 Our analysis reveals different SPE mechanisms operating in the marine boundary layer. The first mode – entrainment
565 zone nucleation – occurs at the boundary layer top (1,200–1,400 m) where several factors create favorable conditions:
566 (1) dilution of mixed-layer air by entrained free tropospheric air causes sudden decreases in preexisting aerosol surface
567 area, (2) adiabatic cooling in rising convective plumes reduces saturation vapor pressures, and (3) turbulent
568 fluctuations in temperature and vapor concentration enhance nucleation rates (Größ et al., 2018; Nilsson et al., 2001).
569 Strong downward fluxes (up to $-41,092 \text{ cm}^{-2} \text{ s}^{-1}$) exceeding the limit of detection confirm that nucleation occurs
570 specifically within this ~ 200 m entrainment layer, while the absence of 3–10 nm particles above the entrainment zone
571 rules out a free tropospheric source. . The limited horizontal extent (2–9 km) of these events is consistent with the
572 spatial scales of organized convective structures that develop in the upper decoupled marine boundary layer following
573 cold front passages in the Azores region, where cumulus-associated drizzle reduces the condensation sink to levels
574 favorable for nucleation (Etling and Brown, 1993; Zheng et al., 2021).

575 The large difference in flux magnitudes between the two entrainment zone events ($-41,092$ vs. $-2,975 \text{ cm}^{-2} \text{ s}^{-1}$)
576 provides information that flux sign alone cannot supply: it reflects spatial heterogeneity in source strength and the
577 proximity of the aircraft to the nucleation zone during each transect. As turbulent intensity is unlikely to have changed
578 substantially over the ~ 1 – 2 hour interval separating the two transects, the order-of-magnitude difference in flux
579 magnitude more plausibly reflects variation in the horizontal distance between the aircraft and the nucleation zone, or
580 spatial heterogeneity in source strength, rather than a change in the turbulent transport efficiency itself. These flux
581 magnitudes, integrated over the duration of the events, represent a substantial source of freshly nucleated particles to
582 the marine aerosol number budget, constraints that can be used directly to evaluate nucleation parameterizations in
583 regional and global models. While the ultimate contribution of these particles to CCN populations depends on growth
584 timescales and loss processes during vertical transport (requiring ~ 24 – 48 hours at typical marine growth rates of ~ 1
585 nm hr^{-1} to reach CCN-relevant sizes; (Zheng et al., 2021)), the flux-based constraints provided here represent a
586 necessary observational foundation for quantifying this contribution in future studies. Our analysis reveals a second
587 distinct mode of SPE occurring within decoupled marine boundary layer structures, where particles originate at the
588 interface between the well-mixed surface layer and the overlying decoupled layer (~ 700 – 800 m altitude). Unlike
589 entrainment zone nucleation, which occurs at the boundary layer top, decoupled layer nucleation operates within the
590 interior of the boundary layer at the interface between the well-mixed surface layer and the overlying stratified layer.
591 Both mechanisms share key preconditions: convergence of air masses with contrasting thermodynamic properties,
592 gradients in potential temperature and water vapor mixing ratio, and aerosol dilution that suppresses the condensation

593 sink. However, the decoupled layer mode is distinguished by stratified vertical mixing that confines turbulent
594 exchange to a narrower altitude range. It is also characterized by a substantially larger horizontal extent (>50 km)
595 compared to entrainment zone events (<10 km), suggesting either more persistent favorable conditions or a
596 fundamentally different source mechanism operating at regional scales. This mode exhibits a regional-scale horizontal
597 extent (>50 km) compared to the localized nature (<10 km) of entrainment zone events. The substantial negative flux
598 magnitudes observed at intermediate altitudes ($-2,782 \text{ cm}^{-2} \text{ s}^{-1}$ at 550 m) combined with positive fluxes aloft
599 demonstrate active particle redistribution throughout the marine boundary layer. The factor of ~ 3 difference in flux
600 magnitude between the 550 m and 30 m levels ($-2,782$ vs. $-860 \text{ cm}^{-2} \text{ s}^{-1}$) is consistent with attenuation of the particle
601 flux during downward transport through dilution with ambient air, as well as losses through coagulation and growth
602 out of the 3–10 nm size range. This vertical divergence in flux magnitude represents a quantitative signature of particle
603 evolution during transport that flux sign alone would be incapable of revealing. This mode represents a significant and
604 previously underappreciated source of secondary marine aerosols that can efficiently contribute to regional aerosol
605 budgets through direct incorporation into the surface mixed layer where particles undergo growth to cloud-relevant
606 sizes.

607 **5. Conclusions**

608 The occurrence of newly formed particles in marine environments has been documented in a number of previous
609 studies. Wiedensohler et al., (1996) observed sub-20 nm particles originating from the free troposphere or cloud tops
610 within the MBL and mixed downwards over the open ocean, suggesting in-situ production based on correlations with
611 absolute humidity. Covert et al., (1992) reported sub-20 nm particle production near precipitating cloud tops within
612 the MBL, where larger particles acting as condensation sinks had been scavenged by precipitation, with sub-20 nm
613 particles dominating 10% of the campaign and indicating episodic rather than continuous production. O'Dowd et al.,
614 (2002) documented NPF events at the coastal Mace Head station when marine air masses encountered biogenic
615 emissions from the intertidal zone. The ACORES campaign, conducted over the Azores at the same time as ACE-
616 ENA, reported freshly nucleated particle bursts near the cloud top exceeding background MBL concentrations by
617 more than an order of magnitude (Siebert et al., 2021). Concurrent helicopter-borne particle flux measurements over
618 the Azores during ACORES (Lückerath et al., 2022) also documented particle fluxes in the marine boundary layer,
619 providing complementary observational context to our aircraft-based approach. The prevailing theoretical framework,
620 based on relatively high sea spray aerosol surface area acting as condensation and coagulation sinks (Bates et al.,
621 1998; Pirjola et al., 2000), nonetheless predicted that NPF should rarely occur in remote marine boundary layers over
622 open oceans. Our flux-based observations build on this existing framework by providing the first direct constraints on
623 the vertical source location and strength of freshly nucleated particles in the remote marine boundary layer. Low
624 aerosol surface area and specific meteorological configurations can create localized or regional zones where conditions
625 become favorable. For entrainment zone and decoupled layer events, extremely low aerosol concentrations, combined
626 with turbulent mixing and adiabatic cooling can create a transient "window" where nucleation can proceed despite
627 moderate surface area concentrations lower in the boundary layer. Recent ground-based observations from the same
628 campaign (Zheng et al., 2021) documented frequent NPF events but could not definitively determine vertical location.

629 Our flux-based approach resolves this ambiguity by providing direct evidence of where particles originate relative to
 630 the measurement location. The negative (downward) fluxes in Case 1 unambiguously demonstrate an above-aircraft
 631 source, while the bidirectional fluxes in Case 2 indicate a distributed source encompassing the measurement altitude.
 632 These findings have important implications for understanding marine aerosol budgets. The spatial scales of these two
 633 SPE modes differ by an order of magnitude: entrainment zone events exhibited limited horizontal extents (<10 km),
 634 consistent with localized convective structures, while decoupled layer events spanned regional scales (50-60 km),
 635 suggesting fundamentally different formation mechanisms or persistence of favorable conditions. For the entrainment
 636 zone mode, while the aircraft sampled the SPE for only ~4 minutes during each transect due to its high ground speed,
 637 NPF events in marine and continental environments are typically observed to persist for 2–5 hours (Islam et al., 2022;
 638 Kulmala et al., 2004; Zheng et al., 2021). Assuming the measured downward flux of $-41,092 \text{ cm}^{-2} \text{ s}^{-1}$ is representative
 639 of a nucleation event of typical duration of ~3 hours and using a mixed layer depth of ~1,200 m, the estimated increase
 640 in vertically integrated particle number concentration is approximately:

$$641 \quad \Delta N_{3-10} \approx |F| \times \frac{\Delta t}{z_{MBL}} = \frac{41,092 \times 10,800}{1.2 \times 10^5} \approx 3,700 \text{ cm}^{-3}$$

642 where F is the flux in $\text{cm}^{-2} \text{ s}^{-1}$, Δt is the event duration in seconds, and z_{MBL} is the mixed layer depth in cm. This
 643 represents a substantial addition to the total particle number concentration in the surface mixed layer, noting that this
 644 estimate refers to freshly nucleated 3–10 nm particles rather than CCN-relevant particles. The fraction surviving to
 645 CCN-relevant sizes (>50–80 nm) depends on growth rates and loss processes that cannot be quantified from single
 646 aircraft transects alone. However, Zheng et al. (2021) estimated that under favorable conditions at the same site, newly
 647 formed particles contributed on average ~50% of total CCN concentrations following cold front passages, suggesting
 648 that even accounting for coagulation losses, the contribution of entrainment zone nucleation to the marine CCN budget
 649 may be substantial. Entrainment zone nucleation, despite its limited horizontal extent, may contribute significantly to
 650 the marine aerosol number budget through sustained downward transport via convective mixing. Though flux
 651 magnitudes for the decoupled layer nucleation events ($-2,782 \text{ cm}^{-2} \text{ s}^{-1}$) are less pronounced, their large spatial extent
 652 likely results in comparable or larger aggregate contributions to regional aerosol budgets. We note that the contribution
 653 of freshly nucleated particles to CCN population depends on growth rates and loss processes during transport and
 654 cannot be assessed from short-term measurements alone. The flux magnitudes and vertical source locations reported
 655 here provide the observational foundation needed to evaluate this contribution quantitatively in future studies
 656 combining particle flux measurements with growth rate and CCN closure analyses.

657 Our observations, combined with combined with the longer history of marine NPF observations cited above and recent
 658 ground-based measurements from the same campaign (Zheng et al., 2021), suggest that the contribution of in-situ
 659 marine boundary layer nucleation to the aerosol budget may be more significant than current model representations
 660 assume. Climate models have historically followed theoretical expectations that marine boundary layer nucleation
 661 should be negligible, instead representing new particles as primarily originating from free tropospheric entrainment
 662 or long-range continental transport (Clarke et al., 2013; Logan et al., 2014), with marine boundary layer nucleation
 663 treated as negligible. The frequent occurrence of SPE during the ACE-ENA campaign (entrainment zone nucleation
 664 in 2 and decoupled layer nucleation in 4 of 39 flights analyzed) suggests that marine boundary layer nucleation – in
 665 both modes – may be more climatologically important than previously recognized. Given that marine boundary layer

666 cloud microphysical properties exhibit the highest sensitivity to aerosol changes (Bellouin et al., 2020; Zhang et al.,
667 2024), and that even modest changes in CCN concentrations can substantially affect cloud radiative forcing in these
668 pristine environments, proper representation of NPF sources is critical for reducing uncertainties in aerosol-cloud
669 interaction estimates.

670 The continuous wavelet transform (CWT) approach proved essential for deriving reliable fluxes from fast-moving
671 aircraft platforms. Traditional eddy covariance methods require stationarity conditions that are difficult to maintain
672 during aircraft sampling, where the platform continuously moves through different air masses. The CWT method's
673 ability to handle non-stationary data while avoiding systematic errors from linear detrending (Rannik and Vesala,
674 1999; Schaller et al., 2017) enabled flux calculations even during complex meteorological conditions. Our detailed
675 analysis of frequency response and flux loss corrections demonstrates that 1 Hz CPC measurements, while not ideal,
676 can resolve sufficient turbulent scales to capture the dominant flux contributions when proper corrections are applied.
677 Importantly, flux magnitudes (not just flux sign) provide essential scientific value: they must exceed the limit of
678 detection to confirm statistical significance, they constrain source strength and proximity, and they provide
679 quantitative inputs for evaluating nucleation parameterizations in regional and global models. As the scientific
680 community works to reduce uncertainties in aerosol-cloud interactions, flux-based approaches offer a promising path
681 forward for understanding how, where, and when new particles form in Earth's remote marine atmosphere.

682 Several limitations warrant acknowledgment. First, our 3–10 nm size range likely misses the initial nucleation at
683 molecular cluster sizes (~1–3 nm), meaning we observe "small particle events" rather than nucleation itself. However,
684 the rapid appearance of 3–10 nm particles with clear vertical structure in turbulent fluxes provides strong indirect
685 evidence for nearby nucleation. Second, the aircraft's high ground speed (~100 m s⁻¹) compared to typical tower-based
686 measurements introduces challenges for capturing the full turbulent spectrum, particularly at lower altitudes where
687 eddy sizes are smaller. Our flux loss corrections (F_m/F ratios of 0.70–0.99) account for this limitation but introduce
688 additional uncertainty. Third, we cannot determine definitively the exact horizontal extent of NPF events from single
689 aircraft transects, though crosswind sampling provides minimum extent estimates.

690 **Future Directions**

691 This work establishes aircraft-derived aerosol fluxes as a valuable tool for characterizing marine boundary layer
692 aerosol sources. Several directions would advance understanding:

693 **Slower aircrafts:** Unmanned aerial vehicles operating at 30–40 m s⁻¹ would better resolve small-scale turbulence,
694 particularly near the surface, where flux loss corrections are currently largest, improving flux accuracy and enabling
695 more detailed vertical structure analysis.

696 **Expanded measurements:** Simultaneous flux measurements of precursor gases (H₂SO₄, NH₃, amines, organics)
697 would directly test hypotheses about nucleation mechanisms and identify which chemical pathways dominate in
698 different scenarios.

699 **Multi-aircraft coordination:** Coordinated measurements from more than one aircraft at different altitudes could
700 directly observe vertical particle transport rates and evolution, constraining growth rates and loss processes during
701 transit.

702 **Longer-term statistics:** Expanding beyond campaign-based measurements to seasonal or annual timescales would
703 quantify the climatological importance of different NPF modes and their relationships to synoptic meteorological
704 patterns.

705 **Model evaluation:** Using observed flux magnitudes and vertical source locations as benchmarks for evaluating marine
706 boundary layer nucleation parameterizations in regional and global models would improve their representation of
707 aerosol-cloud interactions and reduce uncertainties in aerosol indirect forcing estimates.

708 **Code availability**

709 All the scripts used to make the figures used in this study will be available along with the supplementary information

710 **Data availability**

711 All data from the ACE-ENA campaign are archived at the DOE ARM data center, covering measurements from the
712 ARM Aerial Facility near ARM ENA site on Graciosa Island (June 15, 2017 - February 28, 2018).

713 ARM Aerial Facility (AAF) Merged VAP, <https://doi.org/10.5439/1999133>, (AAFMERGED, (Mei and Gaustad,
714 2024)

715 ARM Aerial Facility (AAF) Merged aerosol size distribution, <https://doi.org/10.5439/1905541>,
716 (AAFMERGEDAEROSOLS, (Pekour and Ermold, 2017)

717 ARM Aerial Facility Isokinetic Inlet, <https://doi.org/10.5439/1241544>, (AAFINLETISOK, (Koontz et al., 2016)

718 ARM Aerial Facility (AAF) Aircraft Integrated Meteorological Measurement System (AIMMS) - Meteorological
719 data, <https://doi.org/10.5439/1349241>, (AAFMETAIMS, (Matthews and Goldberger, 2020)

720 Interagency Working Group for Airborne Data and Telemetry Systems,
721 <https://adc.arm.gov/discovery/#/results/s::aaf%20iwg/iopShortName::aaf2017ace-ena>, (IWG ACEENA)

722 Proton Transfer Reaction Mass Spectrometer (PTR-MS),
723 https://adc.arm.gov/discovery/#/results/instrument_code::ptrms/iopShortName::aaf2017ace-ena, (ACE ENA IOP1
724 G1 PTRMS)

725 **Author contribution**

726 ARS, MDP, and NM conceptualized the study. ARS performed the data curation, formal analysis, and designed the
727 figures with contributions from MDP and NM. NM acquired the financial support for the project. ARS and NM wrote
728 the paper, and all authors provided input on the paper for revision before submission.

729 **Competing interests**

730 The authors declare that they have no conflict of interest.

731 **Acknowledgements**

732 We acknowledge the Atmospheric Radiation Measurement (ARM) Climate Research Facility, a user facility of the
733 United States Department of Energy (US DOE), Office of Science, sponsored by the Office of Biological and
734 Environmental Research. We thank Dr. Jian Wang and all the staff responsible for the operation of the ACE-ENA
735 campaign. We acknowledge the use of imagery from the NASA Worldview application, part of the NASA Earth
736 Observing System Data and Information System (EOSDIS). AI tools were used to correct the spelling and sentence
737 structure of the manuscript

738 **Financial support**

739 This work was supported by the DOE Office of Science, Biological and Environment Research, Grant No. DE-
740 SC0024873

741 **References**

742 Andreae, M. O.: Aerosols Before Pollution, *Science*, 315, 50–51, <https://doi.org/10.1126/science.1136529>, 2007.

743 Aubinet, M., Vesala, T., and Papale, D. (Eds.): *Eddy Covariance: A Practical Guide to Measurement and Data*
744 *Analysis*, Springer Netherlands, Dordrecht, <https://doi.org/10.1007/978-94-007-2351-1>, 2012.

745 Bates, T. S., Kapustin, V. N., Quinn, P. K., Covert, D. S., Coffman, D. J., Mari, C., Durkee, P. A., De Bruyn, W. J.,
746 and Saltzman, E. S.: Processes controlling the distribution of aerosol particles in the lower marine boundary layer
747 during the First Aerosol Characterization Experiment (ACE 1), *J. Geophys. Res. Atmospheres*, 103, 16369–16383,
748 <https://doi.org/10.1029/97JD03720>, 1998.

749 Bellouin, N., Quaas, J., Gryspeerdt, E., Kinne, S., Stier, P., Watson-Parris, D., Boucher, O., Carslaw, K. S.,
750 Christensen, M., Daniau, A. -L., Dufresne, J. -L., Feingold, G., Fiedler, S., Forster, P., Gettelman, A., Haywood, J.
751 M., Lohmann, U., Malavelle, F., Mauritsen, T., McCoy, D. T., Myhre, G., Mülmenstädt, J., Neubauer, D., Possner,
752 A., Rugenstein, M., Sato, Y., Schulz, M., Schwartz, S. E., Sourdval, O., Storelvmo, T., Toll, V., Winker, D., and
753 Stevens, B.: Bounding Global Aerosol Radiative Forcing of Climate Change, *Rev. Geophys.*, 58, e2019RG000660,
754 <https://doi.org/10.1029/2019RG000660>, 2020.

755 Boers, R. and Eloranta, E. W.: Lidar measurements of the atmospheric entrainment zone and the potential temperature
756 jump across the top of the mixed layer, *Bound.-Layer Meteorol.*, 34, 357–375, <https://doi.org/10.1007/BF00120988>,
757 1986.

758 Carslaw, K. S., Lee, L. A., Reddington, C. L., Pringle, K. J., Rap, A., Forster, P. M., Mann, G. W., Spracklen, D. V.,
759 Woodhouse, M. T., Regayre, L. A., and Pierce, J. R.: Large contribution of natural aerosols to uncertainty in indirect
760 forcing, *Nature*, 503, 67–71, <https://doi.org/10.1038/nature12674>, 2013.

761 Clarke, A. D., Freitag, S., Simpson, R. M. C., Hudson, J. G., Howell, S. G., Brekhovskikh, V. L., Campos, T.,
762 Kapustin, V. N., and Zhou, J.: Free troposphere as a major source of CCN for the equatorial pacific boundary layer:
763 long-range transport and teleconnections, *Atmospheric Chem. Phys.*, 13, 7511–7529, <https://doi.org/10.5194/acp-13-7511-2013>, 2013.

765 Covert, D. S., Kapustin, V. N., Quinn, P. K., and Bates, T. S.: New particle formation in the marine boundary layer,
766 *J. Geophys. Res. Atmospheres*, 97, 20581–20589, <https://doi.org/10.1029/92JD02074>, 1992.

- 767 Dal Maso, M., Kulmala, M., Riipinen, I., Wagner, R., Hussein, T., Aalto, P. P., and Lehtinen, K.: Formation and
768 growth of fresh atmospheric aerosols: eight years of aerosol size distribution data from SMEAR II, Hyytiälä, Finland,
769 *Boreal Environ. Res.*, 10, 323–336, 2005.
- 770 Deardorff, J. W.: Three-dimensional numerical study of turbulence in an entraining mixed layer, *Bound.-Layer*
771 *Meteorol.*, 7, 199–226, <https://doi.org/10.1007/BF00227913>, 1974.
- 772 Desjardins, R. L., MacPherson, J. I., Schuepp, P. H., and Karanja, F.: An evaluation of aircraft flux measurements of
773 CO₂, water vapor and sensible heat, *Bound.-Layer Meteorol.*, 47, 55–69, 1989.
- 774 Dewani, N., Sakradzija, M., Schlemmer, L., Leinweber, R., and Schmidli, J.: Dependency of vertical velocity variance
775 on meteorological conditions in the convective boundary layer, *Atmospheric Chem. Phys.*, 23, 4045–4058,
776 <https://doi.org/10.5194/acp-23-4045-2023>, 2023.
- 777 Ehn, M., Vuollekoski, H., Petäjä, T., Kerminen, V., Vana, M., Aalto, P., de Leeuw, G., Ceburnis, D., Dupuy, R.,
778 O’Dowd, C. D., and Kulmala, M.: Growth rates during coastal and marine new particle formation in western Ireland,
779 *J. Geophys. Res. Atmospheres*, 115, 2010JD014292, <https://doi.org/10.1029/2010JD014292>, 2010.
- 780 Etling, D. and Brown, R. A.: Roll vortices in the planetary boundary layer: A review, *Bound.-Layer Meteorol.*, 65,
781 215–248, <https://doi.org/10.1007/BF00705527>, 1993.
- 782 Fan, M. and Pekour, M.: CPC_ACEENA, <https://doi.org/10.5439/1440985>, 2018.
- 783 Foken, T., Wimmer, F., Mauder, M., Thomas, C., and Liebethal, C.: Some aspects of the energy balance closure
784 problem, *Atmospheric Chem. Phys.*, 6, 4395–4402, <https://doi.org/10.5194/acp-6-4395-2006>, 2006.
- 785 Galewsky, J., Jensen, M. P., and Delp, J.: Marine Boundary Layer Decoupling and the Stable Isotopic Composition
786 of Water Vapor, *J. Geophys. Res. Atmospheres*, 127, e2021JD035470, <https://doi.org/10.1029/2021JD035470>, 2022.
- 787 Gioli, B., Miglietta, F., De Martino, B., Hutjes, R. W. A., Dolman, H. A. J., Lindroth, A., Schumacher, M., Sanz, M.
788 J., Manca, G., Peressotti, A., and Dumas, E. J.: Comparison between tower and aircraft-based eddy covariance fluxes
789 in five European regions, *Agric. For. Meteorol.*, 127, 1–16, <https://doi.org/10.1016/j.agrformet.2004.08.004>, 2004.
- 790 Glienke, S. and Mei, F.: Two-Dimensional Stereo (2D-S) Probe Instrument Handbook,
791 <https://doi.org/10.2172/1597436>, 2019.
- 792 Größ, J., Hamed, A., Sonntag, A., Spindler, G., Elina Manninen, H., Nieminen, T., Kulmala, M., Hörrak, U., Plass-
793 Dülmer, C., Wiedensohler, A., and Birmili, W.: Atmospheric new particle formation at the research station Melpitz,
794 Germany: connection with gaseous precursors and meteorological parameters, *Atmospheric Chem. Phys.*, 18, 1835–
795 1861, <https://doi.org/10.5194/acp-18-1835-2018>, 2018.
- 796 Helbig, M., Gerken, T., Beamesderfer, E. R., Baldocchi, D. D., Banerjee, T., Biraud, S. C., Brown, W. O. J., Brunzell,
797 N. A., Burakowski, E. A., Burns, S. P., Butterworth, B. J., Chan, W. S., Davis, K. J., Desai, A. R., Fuentes, J. D.,
798 Hollinger, D. Y., Kljun, N., Mauder, M., Novick, K. A., Perkins, J. M., Rahn, D. A., Rey-Sanchez, C., Santanello, J.
799 A., Scott, R. L., Seyednasrollah, B., Stoy, P. C., Sullivan, R. C., de Arellano, J. V.-G., Wharton, S., Yi, C., and
800 Richardson, A. D.: Integrating continuous atmospheric boundary layer and tower-based flux measurements to advance
801 understanding of land-atmosphere interactions, *Agric. For. Meteorol.*, 307, 108509,
802 <https://doi.org/10.1016/j.agrformet.2021.108509>, 2021.
- 803 Hoose, C., Kristjánsson, J. E., Iversen, T., Kirkevåg, A., Seland, Ø., and Gettelman, A.: Constraining cloud droplet
804 number concentration in GCMs suppresses the aerosol indirect effect, *Geophys. Res. Lett.*, 36, 2009GL038568,
805 <https://doi.org/10.1029/2009GL038568>, 2009.
- 806 Horst, T. W.: A Simple Formula for Attenuation of Eddy Fluxes Measured with First-Order Scalar Sensors, *Bound.-*
807 *Layer Meteorol.*, 82, 219–233, <https://doi.org/10.1023/A:1000229130034>, 1997.

808 Intergovernmental Panel on Climate Change (IPCC): Climate Change 2021 – The Physical Science Basis: Working
809 Group I Contribution to the Sixth Assessment Report of the Intergovernmental Panel on Climate Change, 1st ed.,
810 Cambridge University Press, <https://doi.org/10.1017/9781009157896>, 2023.

811 Islam, M. M., Meskhidze, N., Rasheeda Satheesh, A., and Petters, M. D.: Turbulent Flux Measurements of the Near-
812 Surface and Residual-Layer Small Particle Events, *J. Geophys. Res. Atmospheres*, 127, e2021JD036289,
813 <https://doi.org/10.1029/2021JD036289>, 2022.

814 Jones, C. R., Bretherton, C. S., and Leon, D.: Coupled vs. decoupled boundary layers in VOCALS-REx, *Atmospheric*
815 *Chem. Phys.*, 11, 7143–7153, <https://doi.org/10.5194/acp-11-7143-2011>, 2011.

816 Kaimal, J. C. and Finnigan, J. J.: *Atmospheric Boundary Layer Flows: Their Structure and Measurement*, Oxford
817 University Press, <https://doi.org/10.1093/oso/9780195062397.001.0001>, 1994.

818 Koontz, A., Mei, F., and Pekour, M.: *aafinletisok.a1*, <https://doi.org/10.5439/1241544>, 2016.

819 Korolev, A. and Isaac, G. A.: Shattering during Sampling by OAPs and HVPS. Part I: Snow Particles, *J. Atmospheric*
820 *Ocean. Technol.*, 22, 528–542, <https://doi.org/10.1175/JTECH1720.1>, 2005.

821 Kuang, C. and Mei, F.: *Condensation Particle Counter (CPC) Instrument Handbook - Airborne Version*,
822 <https://doi.org/10.2172/1562676>, 2019.

823 Kulkarni, P. and Wang, J.: New fast integrated mobility spectrometer for real-time measurement of aerosol size
824 distribution: II. Design, calibration, and performance characterization, *J. Aerosol Sci.*, 37, 1326–1339,
825 <https://doi.org/10.1016/j.jaerosci.2006.01.010>, 2006a.

826 Kulkarni, P. and Wang, J.: New fast integrated mobility spectrometer for real-time measurement of aerosol size
827 distribution—I: Concept and theory, *J. Aerosol Sci.*, 37, 1303–1325, <https://doi.org/10.1016/j.jaerosci.2006.01.005>,
828 2006b.

829 Kulmala, M., Vehkamäki, H., Petäjä, T., Dal Maso, M., Lauri, A., Kerminen, V.-M., Birmili, W., and McMurry, P.
830 H.: Formation and growth rates of ultrafine atmospheric particles: a review of observations, *J. Aerosol Sci.*, 35, 143–
831 176, <https://doi.org/10.1016/j.jaerosci.2003.10.003>, 2004.

832 Kulmala, M., Petäjä, T., Nieminen, T., Sipilä, M., Manninen, H. E., Lehtipalo, K., Dal Maso, M., Aalto, P. P.,
833 Junninen, H., Paasonen, P., Riipinen, I., Lehtinen, K. E. J., Laaksonen, A., and Kerminen, V.-M.: Measurement of the
834 nucleation of atmospheric aerosol particles, *Nat. Protoc.*, 7, 1651–1667, <https://doi.org/10.1038/nprot.2012.091>, 2012.

835 Lee, X., Massman, W., and Law, B. (Eds.): *Handbook of Micrometeorology: A Guide for Surface Flux Measurement*
836 *and Analysis*, Springer Netherlands, Dordrecht, 250 pp., <https://doi.org/10.1007/1-4020-2265-4>, 2005.

837 Lenschow, D. H. and Stankov, B. B.: Length Scales in the Convective Boundary Layer, *J. Atmospheric Sci.*, 43, 1198–
838 1209, [https://doi.org/10.1175/1520-0469\(1986\)043<1198:LSITCB>2.0.CO;2](https://doi.org/10.1175/1520-0469(1986)043<1198:LSITCB>2.0.CO;2), 1986.

839 Lenschow, D. H., Wulfmeyer, V., and Senff, C.: Measuring Second- through Fourth-Order Moments in Noisy Data,
840 *J. Atmospheric Ocean. Technol.*, 17, 1330–1347, [https://doi.org/10.1175/1520-0426\(2000\)017<1330:MSTFOM>2.0.CO;2](https://doi.org/10.1175/1520-0426(2000)017<1330:MSTFOM>2.0.CO;2), 2000.

842 Li, Y., Wu, Y., Tang, J., Zhu, P., Gao, Z., and Yang, Y.: Quantitative Evaluation of Wavelet Analysis Method for
843 Turbulent Flux Calculation of Non-Stationary Series, *Geophys. Res. Lett.*, 50, e2022GL101591,
844 <https://doi.org/10.1029/2022GL101591>, 2023.

845 Logan, T., Xi, B., and Dong, X.: Aerosol properties and their influences on marine boundary layer cloud condensation
846 nuclei at the ARM mobile facility over the Azores, *J. Geophys. Res. Atmospheres*, 119, 4859–4872,
847 <https://doi.org/10.1002/2013JD021288>, 2014.

- 848 Lückerath, J., Held, A., Siebert, H., Michalkow, M., and Wehner, B.: Vertical aerosol particle exchange in the marine
849 boundary layer estimated from helicopter-borne measurements in the Azores region, *Atmospheric Chem. Phys.*, 22,
850 10007–10021, <https://doi.org/10.5194/acp-22-10007-2022>, 2022.
- 851 Martin, S., Beyrich, F., and Bange, J.: Observing Entrainment Processes Using a Small Unmanned Aerial Vehicle: A
852 Feasibility Study, *Bound.-Layer Meteorol.*, 150, 449–467, <https://doi.org/10.1007/s10546-013-9880-4>, 2014.
- 853 Mather, J. H. and Voyles, J. W.: The Arm Climate Research Facility: A Review of Structure and Capabilities, *Bull.*
854 *Am. Meteorol. Soc.*, 94, 377–392, <https://doi.org/10.1175/BAMS-D-11-00218.1>, 2013.
- 855 Matthews, A. and Goldberger, L.: Aircraft-Integrated Meteorological Measurement System (AIMMS) Instrument
856 Handbook, <https://doi.org/10.2172/1725866>, 2020.
- 857 Mei, F. and Gaustad, K.: ARM Aerial Facility (AAF) Merged Value-Added Product Report for Historical G-1 Field
858 Campaigns, Oak Ridge National Laboratory (ORNL), Oak Ridge, TN (United States). Atmospheric Radiation
859 Measurement (ARM) Data Center, <https://doi.org/10.2172/2335708>, 2024.
- 860 Meskhidze, N., Xu, J., Gantt, B., Zhang, Y., Nenes, A., Ghan, S. J., Liu, X., Easter, R., and Zaveri, R.: Global
861 distribution and climate forcing of marine organic aerosol: 1. Model improvements and evaluation, *Atmospheric*
862 *Chem. Phys.*, 11, 11689–11705, <https://doi.org/10.5194/acp-11-11689-2011>, 2011.
- 863 Meskhidze, N., Jaimes-Correa, J. C., Petters, M. D., Royalty, T. M., Phillips, B. N., Zimmerman, A., and Reed, R.:
864 Possible Wintertime Sources of Fine Particles in an Urban Environment, *J. Geophys. Res. Atmospheres*, 124, 13,055-
865 13,070, <https://doi.org/10.1029/2019JD031367>, 2019.
- 866 Misztal, P. K., Karl, T., Weber, R., Jonsson, H. H., Guenther, A. B., and Goldstein, A. H.: Airborne flux measurements
867 of biogenic isoprene over California, *Atmospheric Chem. Phys.*, 14, 10631–10647, <https://doi.org/10.5194/acp-14-10631-2014>, 2014.
- 869 Modini, R. L., Ristovski, Z. D., Johnson, G. R., He, C., Surawski, N., Morawska, L., Suni, T., and Kulmala, M.: New
870 particle formation and growth at a remote, sub-tropical coastal location, *Atmospheric Chem. Phys.*, 9, 7607–7621,
871 <https://doi.org/10.5194/acp-9-7607-2009>, 2009.
- 872 Nieminen, T., Kerminen, V.-M., Petäjä, T., Aalto, P. P., Arshinov, M., Asmi, E., Baltensperger, U., Beddows, D. C.
873 S., Beukes, J. P., Collins, D., Ding, A., Harrison, R. M., Henzing, B., Hooda, R., Hu, M., Hörrak, U., Kivekäs, N.,
874 Komsaare, K., Krejci, R., Kristensson, A., Laakso, L., Laaksonen, A., Leaitch, W. R., Lihavainen, H., Mihalopoulos,
875 N., Németh, Z., Nie, W., O’Dowd, C., Salma, I., Sellegri, K., Svenningsson, B., Swietlicki, E., Tunved, P., Ulevicius,
876 V., Vakkari, V., Vana, M., Wiedensohler, A., Wu, Z., Virtanen, A., and Kulmala, M.: Global analysis of continental
877 boundary layer new particle formation based on long-term measurements, *Atmospheric Chem. Phys.*, 18, 14737–
878 14756, <https://doi.org/10.5194/acp-18-14737-2018>, 2018.
- 879 Nilsson, E. D., Rannik, Ü., Kulmala, M., Buzorius, G., and O’Dowd, C. D.: Effects of continental boundary layer
880 evolution, convection, turbulence and entrainment, on aerosol formation, *Tellus Ser. B Chem. Phys. Meteorol. B*, 53,
881 441–461, <https://doi.org/10.3402/tellusb.v53i4.16617>, 2001.
- 882 Novak, G. A., Fite, C. H., Holmes, C. D., Veres, P. R., Neuman, J. A., Faloona, I., Thornton, J. A., Wolfe, G. M.,
883 Vermeuel, M. P., Jernigan, C. M., Peischl, J., Ryerson, T. B., Thompson, C. R., Bourgeois, I., Warneke, C., Gkatzelis,
884 G. I., Coggon, M. M., Sekimoto, K., Bui, T. P., Dean-Day, J., Diskin, G. S., DiGangi, J. P., Nowak, J. B., Moore, R.
885 H., Wiggins, E. B., Winstead, E. L., Robinson, C., Thornhill, K. L., Sanchez, K. J., Hall, S. R., Ullmann, K., Dollner,
886 M., Weinzierl, B., Blake, D. R., and Bertram, T. H.: Rapid cloud removal of dimethyl sulfide oxidation products limits
887 SO₂ and cloud condensation nuclei production in the marine atmosphere, *Proc. Natl. Acad. Sci.*, 118, e2110472118,
888 <https://doi.org/10.1073/pnas.2110472118>, 2021.
- 889 O’Dowd, C., Monahan, C., and Dall’Osto, M.: On the occurrence of open ocean particle production and growth events,
890 *Geophys. Res. Lett.*, 37, 2010GL044679, <https://doi.org/10.1029/2010GL044679>, 2010.

891 O'Dowd, C. D., Hämeri, K., Mäkelä, J., Väkeva, M., Aalto, P., de Leeuw, G., Kunz, G. J., Becker, E., Hansson, H.,
892 Allen, A. G., Harrison, R. M., Berresheim, H., Kleefeld, C., Geever, M., Jennings, S. G., and Kulmala, M.: Coastal
893 new particle formation: Environmental conditions and aerosol physicochemical characteristics during nucleation
894 bursts, *J. Geophys. Res. Atmospheres*, 107, <https://doi.org/10.1029/2000JD000206>, 2002.

895 Olfert, J. S., Kulkarni, P., and Wang, J.: Measuring aerosol size distributions with the fast integrated mobility
896 spectrometer, *J. Aerosol Sci.*, 39, 940–956, <https://doi.org/10.1016/j.jaerosci.2008.06.005>, 2008.

897 Pekour, M. and Ermold, B.: ARM Aerial Facility (AAF) Merged aerosol size distribution,
898 <https://doi.org/10.5439/1905541>, 2017.

899 Petters, M. D., Snider, J. R., Stevens, B., Vali, G., Faloona, I., and Russell, L. M.: Accumulation mode aerosol, pockets
900 of open cells, and particle nucleation in the remote subtropical Pacific marine boundary layer, *J. Geophys. Res.*
901 *Atmospheres*, 111, 2004JD005694, <https://doi.org/10.1029/2004JD005694>, 2006.

902 Pirjola, L., O'Dowd, C. D., Brooks, I. M., and Kulmala, M.: Can new particle formation occur in the clean marine
903 boundary layer?, *J. Geophys. Res. Atmospheres*, 105, 26531–26546, <https://doi.org/10.1029/2000JD900310>, 2000.

904 Pope, S. B.: *Turbulent Flows*, 1st ed., Cambridge University Press, <https://doi.org/10.1017/CBO9780511840531>,
905 2000.

906 Pryor, S. C., Larsen, S. E., Sørensen, L. L., Barthelmie, R. J., Grönholm, T., Kulmala, M., Launiainen, S., Rannik, Ü.,
907 and Vesala, T.: Particle fluxes over forests: Analyses of flux methods and functional dependencies, *J. Geophys. Res.*,
908 112, D07205, <https://doi.org/10.1029/2006JD008066>, 2007.

909 Quinn, P. K., Coffman, D. J., Johnson, J. E., Upchurch, L. M., and Bates, T. S.: Small fraction of marine cloud
910 condensation nuclei made up of sea spray aerosol, *Nat. Geosci.*, 10, 674–679, <https://doi.org/10.1038/ngeo3003>, 2017.

911 Rannik, Ü. and Vesala, T.: Autoregressive filtering versus linear detrending in estimation of fluxes by the eddy
912 covariance method, *Bound.-Layer Meteorol.*, 91, 259–280, <https://doi.org/10.1023/A:1001840416858>, 1999.

913 Sakai, R. K., Fitzjarrald, D. R., and Moore, K. E.: Importance of Low-Frequency Contributions to Eddy Fluxes
914 Observed over Rough Surfaces, *J. Appl. Meteorol.*, 40, 2178–2192, [https://doi.org/10.1175/1520-0450\(2001\)040<2178:IOLFCT>2.0.CO;2](https://doi.org/10.1175/1520-0450(2001)040<2178:IOLFCT>2.0.CO;2), 2001.

916 Sanchez, K. J., Zhang, B., Liu, H., Saliba, G., Chen, C.-L., Lewis, S. L., Russell, L. M., Shook, M. A., Crosbie, E. C.,
917 Ziemba, L. D., Brown, M. D., Shingler, T. J., Robinson, C. E., Wiggins, E. B., Thornhill, K. L., Winstead, E. L.,
918 Jordan, C., Quinn, P. K., Bates, T. S., Porter, J., Bell, T. G., Saltzman, E. S., Behrenfeld, M. J., and Moore, R. H.:
919 Linking marine phytoplankton emissions, meteorological processes, and downwind particle properties with
920 FLEXPART, *Atmospheric Chem. Phys.*, 21, 831–851, <https://doi.org/10.5194/acp-21-831-2021>, 2021.

921 Schaller, C., Göckede, M., and Foken, T.: Flux calculation of short turbulent events – comparison of three methods,
922 *Atmospheric Meas. Tech.*, 10, 869–880, <https://doi.org/10.5194/amt-10-869-2017>, 2017.

923 Schmid, B., Tomlinson, J. M., Hubbe, J. M., Comstock, J. M., Mei, F., Chand, D., Pekour, M. S., Kluzek, C. D.,
924 Andrews, E., Biraud, S. C., and McFarquhar, G. M.: The DOE ARM Aerial Facility, *Bull. Am. Meteorol. Soc.*, 95,
925 723–742, <https://doi.org/10.1175/BAMS-D-13-00040.1>, 2014.

926 Siebert, H., Szodry, K.-E., Egerer, U., Wehner, B., Henning, S., Chevalier, K., Lückerath, J., Welz, O., Weinhold, K.,
927 Lauermaun, F., Gottschalk, M., Ehrlich, A., Wendisch, M., Fialho, P., Roberts, G., Allwayin, N., Schum, S., Shaw,
928 R. A., Mazzoleni, C., Mazzoleni, L., Nowak, J. L., Malinowski, S. P., Karpinska, K., Kumala, W., Czyzewska, D.,
929 Luke, E. P., Kollias, P., Wood, R., and Mellado, J. P.: Observations of Aerosol, Cloud, Turbulence, and Radiation
930 Properties at the Top of the Marine Boundary Layer over the Eastern North Atlantic Ocean: The ACORES Campaign,
931 *Bull. Am. Meteorol. Soc.*, 102, E123–E147, <https://doi.org/10.1175/BAMS-D-19-0191.1>, 2021.

- 932 Spirig, C., Neftel, A., Ammann, C., Dommen, J., Grabmer, W., Thielmann, A., Schaub, A., Beauchamp, J., Wisthaler,
933 A., and Hansel, A.: Eddy covariance flux measurements of biogenic VOCs during ECHO 2003 using proton transfer
934 reaction mass spectrometry, *Atmospheric Chem. Phys.*, 5, 465–481, <https://doi.org/10.5194/acp-5-465-2005>, 2005.
- 935 Stull, R. B. (Ed.): *An Introduction to Boundary Layer Meteorology*, Springer Netherlands, Dordrecht,
936 <https://doi.org/10.1007/978-94-009-3027-8>, 1988.
- 937 Sun, Y., Jia, L., Chen, Q., and Zheng, C.: Optimizing Window Length for Turbulent Heat Flux Calculations from
938 Airborne Eddy Covariance Measurements under Near Neutral to Unstable Atmospheric Stability Conditions, *Remote
939 Sens.*, 10, 670, <https://doi.org/10.3390/rs10050670>, 2018.
- 940 Torrence, C. and Compo, G. P.: A Practical Guide to Wavelet Analysis., *Bull. Am. Meteorol. Soc.*, 79, 61–78,
941 [https://doi.org/10.1175/1520-0477\(1998\)079<0061:APGTWA>2.0.CO;2](https://doi.org/10.1175/1520-0477(1998)079<0061:APGTWA>2.0.CO;2), 1998.
- 942 Wang, J., Pikridas, M., Spielman, S. R., and Pinterich, T.: A fast integrated mobility spectrometer for rapid
943 measurement of sub-micrometer aerosol size distribution, Part I: Design and model evaluation, *J. Aerosol Sci.*, 108,
944 44–55, <https://doi.org/10.1016/j.jaerosci.2017.02.012>, 2017a.
- 945 Wang, J., Pikridas, M., Pinterich, T., Spielman, S. R., Tsang, T., McMahon, A., and Smith, S.: A Fast Integrated
946 Mobility Spectrometer for rapid measurement of sub-micrometer aerosol size distribution, Part II: Experimental
947 characterization, *J. Aerosol Sci.*, 113, 119–129, <https://doi.org/10.1016/j.jaerosci.2017.05.001>, 2017b.
- 948 Wang, J., Wood, R., Jensen, M., Azevedo, E., Bretherton, C., and Chand, D.: *Aerosol and Cloud Experiments in
949 Eastern North Atlantic (ACE-ENA) Field Campaign Report*, 2019.
- 950 Weber, R. J., Marti, J. J., McMurry, P. H., Eisele, F. L., Tanner, D. J., and Jefferson, A.: Measurements of new particle
951 formation and ultrafine particle growth rates at a clean continental site, *J. Geophys. Res. Atmospheres*, 102, 4375–
952 4385, <https://doi.org/10.1029/96JD03656>, 1997.
- 953 Weber, R. J., Clarke, A. D., Litchy, M., Li, J., Kok, G., Schillawski, R. D., and McMurry, P. H.: Spurious aerosol
954 measurements when sampling from aircraft in the vicinity of clouds, *J. Geophys. Res. Atmospheres*, 103, 28337–
955 28346, <https://doi.org/10.1029/98JD02086>, 1998.
- 956 Wiedensohler, A., Covert, D. S., Swietlicki, Erik., Aalto, Pasi., Heintzenberg, Jost., and Leck, C.: Occurrence of an
957 ultrafine particle mode less than 20 nm in diameter in the marine boundary layer during Arctic summer and autumn,
958 *Tellus B*, 48, 213–222, <https://doi.org/10.1034/j.1600-0889.1996.t01-1-00006.x>, 1996.
- 959 Wolfe, G. M., Kawa, S. R., Hanisco, T. F., Hannun, R. A., Newman, P. A., Swanson, A., Bailey, S., Barrick, J.,
960 Thornhill, K. L., Diskin, G., DiGangi, J., Nowak, J. B., Sorenson, C., Bland, G., Yungel, J. K., and Swenson, C. A.:
961 The NASA Carbon Airborne Flux Experiment (CARAFE): instrumentation and methodology, *Atmospheric Meas.
962 Tech.*, 11, 1757–1776, <https://doi.org/10.5194/amt-11-1757-2018>, 2018.
- 963 Wood, R. and Bretherton, C. S.: Boundary Layer Depth, Entrainment, and Decoupling in the Cloud-Capped
964 Subtropical and Tropical Marine Boundary Layer, *J. Clim.*, 17, 3576–3588, [https://doi.org/10.1175/1520-0442\(2004\)017<3576:BLDEAD>2.0.CO;2](https://doi.org/10.1175/1520-0442(2004)017<3576:BLDEAD>2.0.CO;2), 2004.
- 966 Wood, R., Wyant, M., Bretherton, C. S., Rémillard, J., Kollias, P., Fletcher, J., Stemmler, J., de Szoeko, S., Yuter, S.,
967 Miller, M., Mechem, D., Tselioudis, G., Chiu, J. C., Mann, J. A. L., O’Connor, E. J., Hogan, R. J., Dong, X., Miller,
968 M., Ghate, V., Jefferson, A., Min, Q., Minnis, P., Palikonda, R., Albrecht, B., Luke, E., Hannay, C., and Lin, Y.:
969 Clouds, Aerosols, and Precipitation in the Marine Boundary Layer: An Arm Mobile Facility Deployment, *Bull. Am.
970 Meteorol. Soc.*, 96, 419–440, <https://doi.org/10.1175/BAMS-D-13-00180.1>, 2015.
- 971 Wulfmeyer, V., Muppa, S. K., Behrendt, A., Hammann, E., Späth, F., Sorbjan, Z., Turner, D. D., and Hardesty, R.
972 M.: Determination of Convective Boundary Layer Entrainment Fluxes, Dissipation Rates, and the Molecular

973 Destruction of Variances: Theoretical Description and a Strategy for Its Confirmation with a Novel Lidar System
974 Synergy, *J. Atmospheric Sci.*, 73, 667–692, <https://doi.org/10.1175/JAS-D-14-0392.1>, 2016.

975 Yoon, Y. J. and Brimblecombe, P.: Modelling the contribution of sea salt and dimethyl sulfide derived aerosol to
976 marine CCN, *Atmospheric Chem. Phys.*, 2, 17–30, <https://doi.org/10.5194/acp-2-17-2002>, 2002.

977 Zhang, J., Chen, Y.-S., Yamaguchi, T., and Feingold, G.: Cloud water adjustments to aerosol perturbations are
978 buffered by solar heating in non-precipitating marine stratocumuli, *Atmospheric Chem. Phys.*, 24, 10425–10440,
979 <https://doi.org/10.5194/acp-24-10425-2024>, 2024.

980 Zheng, G., Wang, Y., Aiken, A. C., Gallo, F., Jensen, M. P., Kollias, P., Kuang, C., Luke, E., Springston, S., Uin, J.,
981 Wood, R., and Wang, J.: Marine boundary layer aerosol in the eastern North Atlantic: seasonal variations and key
982 controlling processes, *Atmospheric Chem. Phys.*, 18, 17615–17635, <https://doi.org/10.5194/acp-18-17615-2018>,
983 2018.

984 Zheng, G., Wang, Y., Wood, R., Jensen, M. P., Kuang, C., McCoy, I. L., Matthews, A., Mei, F., Tomlinson, J. M.,
985 Shilling, J. E., Zawadowicz, M. A., Crosbie, E., Moore, R., Ziemba, L., Andreae, M. O., and Wang, J.: New particle
986 formation in the remote marine boundary layer, *Nat. Commun.*, 12, 527, [https://doi.org/10.1038/s41467-020-20773-](https://doi.org/10.1038/s41467-020-20773-1)
987 1, 2021.

988